TECHNISCHE
UNIVERSITÄT
WIEN
Vienna University of Technology

DIPLOMARBEIT

Development and assessment of a calorimeter data acquisition and evaluation software for ionizing particles

zur Erlangung des akademischen Grades

Diplom-Ingenieur

im Rahmen des Studiums

Technische Physik

eingereicht von

Benjamin Huber BSc
Matrikelnummer: 01326034

ausgeführt am Atominstitut
der Fakultät für Physik der Technischen Universität Wien

Betreuung
Betreuer: Privatdoz. Dipl.-Ing. Dr.techn. Christoph Schwanda
Mitwirkung: Univ.Lektor Dipl.-Ing. Dr.techn. Thomas Bergauer

Wien, 21.10.2020

(Unterschrift Verfasser/in) (Unterschrift Betreuer/in)

Abstract

Hadrontherapy, the irradiation of cancerous tissue with ions, is an already well established medical treatment, as it affects less healthy tissue than conventional radiotherapy due to the very localized energy deposition of accelerated ions. Yet, treatment planning is still done with conventional computer tomography, which has the drawback of a required conversion that is still slightly inaccurate. A direct proton computer tomography (pCT) would eliminate the need for such conversion. With the recently opened MedAustron in Wiener Neustadt the HEPHY Vienna has thus started researching into a demonstrative pCT set-up. In this project a measurement software for the calorimeter, that measures the residual energy of protons, has been developed. The software allows for automatized evaluation including pedestal subtraction and automatic calibration, offers various live data visualizations and produces output files that are easy to work with in Python or CERN's ROOT framework. The evaluation measurements with this new software have been conducted at the HEPHY and at MedAustron and have provided more insight in the current state of the calorimeter. Especially the two modes, range telescope and sampling calorimeter have been assessed, and it has been found that only the range telescope mode is feasible in the current state of the calorimeter. It has further been shown that this is due to resolution problems in the proximity of the Bragg peak that are difficult to correct. Additionally, a new combined single proton range determination method has been proposed, compared and discussed. This method is a combination of the standard "last slice over threshold method" and a proposed "first slice under threshold minus one" method. The combined method overall exhibits the smallest deviations from the expected range.

Kurzfassung

Hadronentherapie, die Bestrahlung von Tumorgewebe mit Ionen, ist eine bereits gut etablierte medizinische Behandlung, da sie gesundes Gewebe besser schont als konventionelle Strahlentherapie, aufgrund der sehr lokalisierten Energieabgabe beschleunigter Ionen. Die Behandlungsplanung greift jedoch immer noch auf herkömmliche Computertomographie zurück, die den Nachteil einer benötigten Umrechnung, welche immer noch leicht ungenau ist, mit sich bringt. Eine direkte Computertomographie mit Protonen (pCT) würde diese Umrechnung obsolet machen. Mit dem kürzlich eröffneten MedAustron in Wiener Neustadt hat das HEPHY Wien daher ein Projekt zur Erforschung eines konzeptionellen pCT Aufbaus gestartet. In diesem Projekt wurde eine Messsoftware für das Kalorimeter, das zur Bestimmung der Protonenrestenergie verwendet wurde, entwickelt. Die Software beinhält automatisierte Datenauswertung in Form von Pedestalsubstraktion und automatisierter Kalibration, zahlreiche Optionen zur Echtzeitdatenvisualisierung und erzeugt Dateien die mittels Python oder CERNs ROOT-Framework einfach auswertbar sind. Die Evaluierungsexperimente mit der neuen Software wurden am HEPHY und am MedAustron durchgeführt und lieferten einen besseren Einblick in den derzeitigen Stand des Kalorimeters. Besonders die beiden Modi, Range-Telescope und Sampling-Kalorimeter wurden diskutiert. Dabei wurde festgestellt, dass das Kalorimeter derzeit zuverlässig nur im Range-Telescope-Modus betrieben werden kann. Es wurde gezeigt, dass dies mit den Auflösungsproblemen in der Nähe des Bragg-Peaks zusammenhängt, welche schwierig zu korrigieren sind. Des Weiteren wurde eine neue Kombinationsmethode zur Bestimmung der Eindringtiefe von einzelnen Protonen im Kalorimeter vorgeschlagen, diskutiert und verglichen. Diese ist eine Kombination der "last slice over threshold"-Methode sowie einer "first slice under threshold minus one"-Methode. Die Kombinationsmethode zeigte die kleinsten Abweichungen von der erwarteten Eindringtiefe einzelner Protonen im Kalorimeter.

Contents

1 Introduction

In 2016 the MedAustron [1] in Wiener Neustadt opened for patient treatment. Its main purpose is to offer hadrontherapy, which is a form of cancer treatment via high energy ionizing particles like protons and carbon nuclei. As opposed to conventional radiotherapy, hadrontherapy affects substantially less healthy tissue and is especially of interest for various tumours that are difficult to reach via surgery. One crucial part of hadrontherapy is treatment planning, which involves imaging the cancerous tissue together with its surroundings, currently via means of x-ray computer tomography and from this calculating the positions and energies for ion irradiation. However, the problem with this approach is that there is a small but non-negligible uncertainty of $\sim 3\%$ [2] when converting from the x-ray's Hounsfield units to ion stopping power. This uncertainty can be lowered when the imaging is similarly to the treatment done with high energy ions of lower intensity [3].

There is thus worldwide ongoing research into proton computer tomography (pCT), with a growing involvement of the institute of high energy physics in Vienna [4]. Proton computer tomography would function very similar to standard x-ray computer tomography, where the target is irradiated from different angles and the recorded residual energy can then be used to reconstruct a 3D image [5]. The contrast within the image however, would correspond to the varying proton stopping power of the material. The current set-up consists of the proton beam at MedAustron, two trackers, one in front of the target and one behind, as well as a calorimeter that measures the residual beam energy.

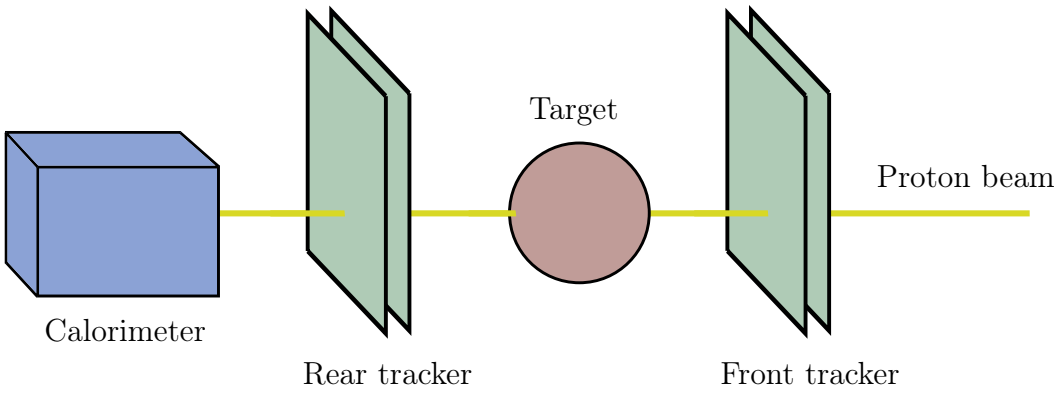

Figure 1: Schematic drawing of the proton CT set-up.

My work in this project focused on the software for the TERA calorimeter [6]. It involved porting the existing LabView software to C++, which can then be compiled and executed on a PC running the Linux operating system. This consequently also allowed us to use existing software packages like CERN's ROOT framework [7] to automatize certain stages of the data evaluation.

The results of the first evaluation measurements with this new software shall be presented in this report.

2 Theory

2.1 Energy loss of charged particles traversing matter

2.1.1 Semi-classical derivation

The mechanism of energy loss of fast charged particles that traverse a material of a given thickness was first studied by Nils Bohr in 1913 [8]. He came up with a classical derivation of an energy loss function which describes how fast particles lose energy by exciting atomic electrons. To derive this function, we start by considering the momentum transfer of a moving charged particle onto a single atomic electron. On its path the moving particle with mass M and charge ze may be a distance $r(t)$ apart from an atomic electron with mass m and charge $-e$ (Fig. 2).

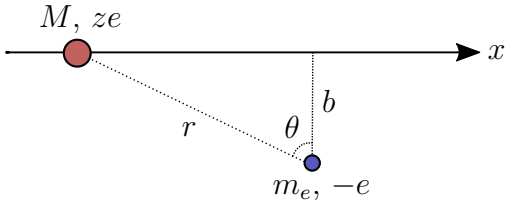

Figure 2: Schematic drawing of an incident particle (M, ze) on a trajectory that is close to an electron (m_e, $-e$) with a minimum distance b (impact parameter).

We can write the momentum transferred as the integral over the Coulomb force that these two particles exert on each other

$$\Delta p = \int_{-\infty}^{\infty} F_{Coulomb}\ \mathrm{d}t = \int_{-\infty}^{\infty} -\frac{ze^2}{4\pi\epsilon_0 r^2}\ \mathrm{d}t \quad . \tag{2.1}$$

We neglect any electron or incident particle movement perpendicular to the x-axis during the interaction as the time for it is assumed to be very short. Thus, we can easily see that the total contribution of the longitudinal component $F_{\parallel,\,Coulomb}$ cancels as $F_{\parallel,\,Coulomb}(x) = -F_{\parallel,\,Coulomb}(-x)$. Hence, by now only considering the transversal component, we can rewrite Eq. 2.1 as[1]

$$\Delta p = \int_{-\infty}^{\infty} F_{\perp,\,Coulomb}\ \mathrm{d}t = \int_{-\infty}^{\infty} -\frac{ze^2}{4\pi\epsilon_0 r^2}\cos(\theta)\ \frac{\mathrm{d}x}{v} \quad . \tag{2.2}$$

Using trigonometry one obtains $r \cdot \cos(\theta) = b$ and $x = b \cdot \tan(\theta)$. From the latter we can work out $\mathrm{d}x = \frac{b}{\cos^2(\theta)}\ \mathrm{d}\theta$. Using those identities we can now express the momentum transfer as an integral over the angle θ,

$$\Delta p = -\frac{ze^2}{4\pi\epsilon_0 b^2 v}\int_{-\pi/2}^{\pi/2}\cos^3(\theta)\ \frac{b\cdot\mathrm{d}\theta}{\cos^2(\theta)} = -\frac{2ze^2}{4\pi\epsilon_0 bv} \quad . \tag{2.3}$$

[1] The integral $\int_{-\infty}^{\infty} F_{\perp,\,Coulomb}\ \mathrm{d}t$ remains unchanged when expressed relativistically as $F_{\perp,\,Coulomb} \to \gamma F_{\perp,\,Coulomb}$ and $\mathrm{d}t \to \mathrm{d}t/\gamma$.

Let us now assume that the energy $\Delta E = \Delta p^2/2m_e$, transferred via this mechanism to the electron[2], is ultimately lost to the incident particle as the energy is used to excite the atomic electron into a higher energy state[3],

$$\Delta E = \frac{\Delta p^2}{2m_e} = \left(\frac{e^2}{4\pi\epsilon_0}\right)^2 \cdot \frac{2z^2}{m_e b^2 v^2} \quad . \tag{2.4}$$

Instead of considering only one electron we now consider the number of electrons in a cylindrical shell of radius b, thickness $\mathrm{d}b$ and length $\mathrm{d}x$ (Fig. 3).

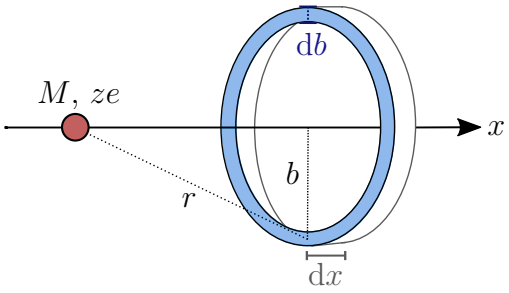

Figure 3: Schematic drawing of a particle $(M,\ ze)$ traversing a cylindrical electron shell.

With the electron density n_e we obtain for the number of electrons in the shell

$$N_e = 2\pi b n_e \,\mathrm{d}b\,\mathrm{d}x \quad . \tag{2.5}$$

Hence, the transferred energy to electrons in such an infinitesimal shell becomes

$$\mathrm{d}E(b) = \left(\frac{e^2}{4\pi\epsilon_0}\right)^2 \cdot \frac{4\pi z^2 n_e}{m_e v^2} \cdot \frac{\mathrm{d}b}{b}\,\mathrm{d}x \quad . \tag{2.6}$$

To get the contribution of all shells in the range of b_{min} to b_{max}, we integrate Eq. 2.6 with respect to $\mathrm{d}b$

$$\frac{\mathrm{d}E}{\mathrm{d}x} = \left(\frac{e^2}{4\pi\epsilon_0}\right)^2 \cdot \frac{4\pi z^2 n_e}{m_e v^2} \int_{b_{min}}^{b_{max}} \frac{\mathrm{d}b}{b} = \left(\frac{e^2}{4\pi\epsilon_0}\right)^2 \cdot \frac{4\pi z^2 n_e}{m_e v^2} \ln\left(\frac{b_{max}}{b_{min}}\right) \quad . \tag{2.7}$$

The lower limit b_{min} corresponds to the maximal possible energy transfer, which is the case for a head on collision, for which the energy transfer can be calculated using relativistic

[2]As Δp will further be assumed to be infinitesimal $\Delta E = \Delta p^2/2m_e$ does not change when expanded relativistically $\Delta E = \Delta E_{tot} - m_e c^2 = \sqrt{\Delta p^2 c^2 - m_e^2 c^4} - m_e c^2 \approx m_e c^2 - m_e c^2 + \Delta p^2 \cdot \frac{1}{2m_e}$.

[3]In his original work Bohr also considered the displacement of the electron due to the transversal and longitudinal forces that act on it. This gave him a factor $P(x)$ in Eq. 2.4 and an additional term $\propto \ln(k)$ with $k = 1.123$ in the end result Eq. 2.13. This term loosely corresponds to the later developed shell correction in the quantum mechanical version. For this simple approximation we neglect it.

kinematics (Appendix A.1) and yields

$$\Delta E(b_{min}) = W_{max} = \frac{2m_e\gamma^2v^2}{1 + 2\gamma\frac{m_e}{M} + \left(\frac{m_e}{M}\right)^2} \quad . \tag{2.8}$$

It should be noted that if $M \gg 2\gamma m_e$, which is the case for hadronic incident particles (e.g. protons), whose velocity is not too close to c, we can simplify Eq. 2.8 further to obtain

$$W_{max} \approx 2m_e\gamma^2v^2 \quad . \tag{2.9}$$

Plugging Eq. 2.8 into Eq. 2.4 and solving for b yields

$$b_{min} = \frac{e^2}{4\pi\epsilon_0} \cdot \sqrt{\frac{2z^2}{v^2 m_e W_{max}}} \quad . \tag{2.10}$$

Similarly, b_{max} corresponds to the minimal possible energy transfer. Classically this energy transfer may be arbitrarily small, yet quantum mechanics only allows discrete energy transfers. The cumbersome quantum mechanically calculation yields [9]

$$\Delta E(b_{max}) = \frac{I^2}{2\gamma^2 v^2 m_e} \quad . \tag{2.11}$$

Where I is the mean ionization potential within the material. By using Eq. 2.4 again we obtain

$$b_{max} = \frac{e^2}{4\pi\epsilon_0} \cdot \sqrt{\frac{4\gamma^2 z^2}{I^2}} \quad . \tag{2.12}$$

Plugging Eq. 2.10 and Eq. 2.12 into Eq. 2.7 and instead of considering the energy gained by the electrons we now consider the energy lost by the incident particle we finally find

$$-\frac{\mathrm{d}E}{\mathrm{d}x} = \left(\frac{e^2}{4\pi\epsilon_0}\right)^2 \cdot \frac{2\pi z^2 n_e}{m_e v^2} \ln\left(\frac{2\gamma^2 v^2 m_e W_{max}}{I^2}\right) \quad . \tag{2.13}$$

2.1.2 Bethe formula

Eq. 2.13 is the semi-classical approximation for the quantum mechanical version that was first derived in 1930 by Hans Bethe using non-relativistic quantum mechanics [10]. Two years later he additionally employed the relativistic Dirac equation to derive what it is now known as the **Bethe formula** of stopping power (often also referred to as Bethe-Bloch formula) [11, 12]

$$-\frac{\mathrm{d}E}{\mathrm{d}x} = \left(\frac{e^2}{4\pi\epsilon_0}\right)^2 \cdot \frac{2\pi z^2 n_e}{m_e v^2} \left[\ln\left(\frac{2\gamma^2 v^2 m_e W_{max}}{I^2}\right) - 2\beta^2\right] \quad . \tag{2.14}$$

2.1.3 Correction terms

Later, correction terms were added to Eq. 2.14 [12, 13]

$$-\frac{\mathrm{d}E}{\mathrm{d}x} = \left(\frac{e^2}{4\pi\epsilon_0}\right)^2 \cdot \frac{2\pi z^2 n_e}{m_e v^2} \left[\ln\left(\frac{2\gamma^2 v^2 m_e W_{max}}{I^2}\right) - 2\beta^2 - \underbrace{\delta(\beta\gamma)}_{\substack{\text{Density}\\\text{correction}}} - \underbrace{2\frac{C}{Z}}_{\substack{\text{Shell}\\\text{correction}}}\right] \quad . \tag{2.15}$$

Where the **density correction** is an effect that becomes significant at higher energies ($\sim 1\,\mathrm{GeV}$ for muons). The effect is due to the relativistic prolongation of the Coulomb force $\gamma F_{\perp,Coulomb}$ that is mitigated by the polarization of the material. This forces the $\propto \ln(\gamma^2 v^2)$ growth into a $\propto \ln(\gamma v)$ growth in that regime.

The **shell correction** summarizes a couple of effects that take the movement of the electrons, the deformation of their shells as well as the screening of lower shells into account. These effects become significant at lower energies ($\beta < 0.3$).

Eq. 2.15 very accurately describes the stopping power of charged particles in matter in the range of $\sim 50\,\mathrm{keV}$ (muons) to $\sim 50\,\mathrm{GeV}$ (muons). Above this range the radiative energy loss starts to dominate. Moreover, light particles like electrons mainly loose energy via radiative energy loss, specifically via Bremsstrahlung.

There are a number of additional effects that affect the particles' energy loss such as Cherenkov radiation, nuclear reactions or Coulomb scattering by the nuclei. These effects only have a comparably small influence on the energy loss. However, nuclear Coulomb scattering for example is of significance for a different reason. It is the main cause for radiation damage in the material that is being irradiated, through the creation of vacancies and interstitials. This is especially of interest for less radiation hard materials like plastic scintillators.

2.1.4 Minimum ionizing particles (MIPs)

The stopping power (Eq. 2.14) has a minimum at roughly $\beta\gamma \sim 2\sqrt{2}$. Since most relevant particles and materials show a similar stopping power around this point, particularly

$$-\frac{\mathrm{d}E}{\mathrm{d}x} \approx \rho \cdot 2\,\frac{\mathrm{MeVcm}^2}{\mathrm{g}} \quad , \tag{2.16}$$

particles with such a momentum ($\beta\gamma = p/Mc$) are grouped together under the term minimum ionizing particles (MIPs).

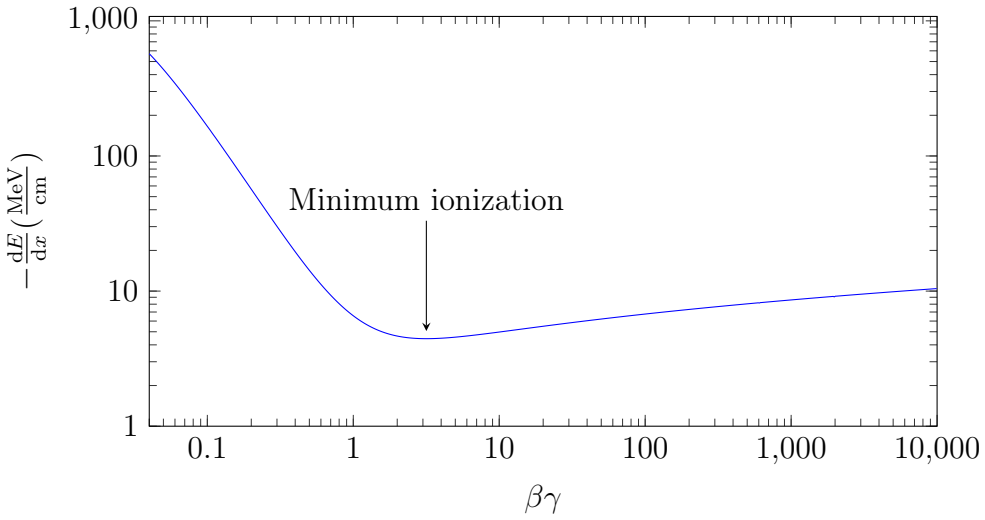

Figure 4: Stopping power of protons in aluminium as a function of the reduced proton momentum $\beta\gamma = p/Mc$ (calculated via Eq. 2.14).

2.1.5 Bragg curve

One important fact about the Bethe formula (Eq. 2.14) is that for $\beta \ll 1$ it is $\propto 1/v^2$, which implies that the energy deposition reaches a maximum just before the incident particles come to rest. The resulting peak is known as Bragg peak after William Henry Bragg who first discovered it in 1903.

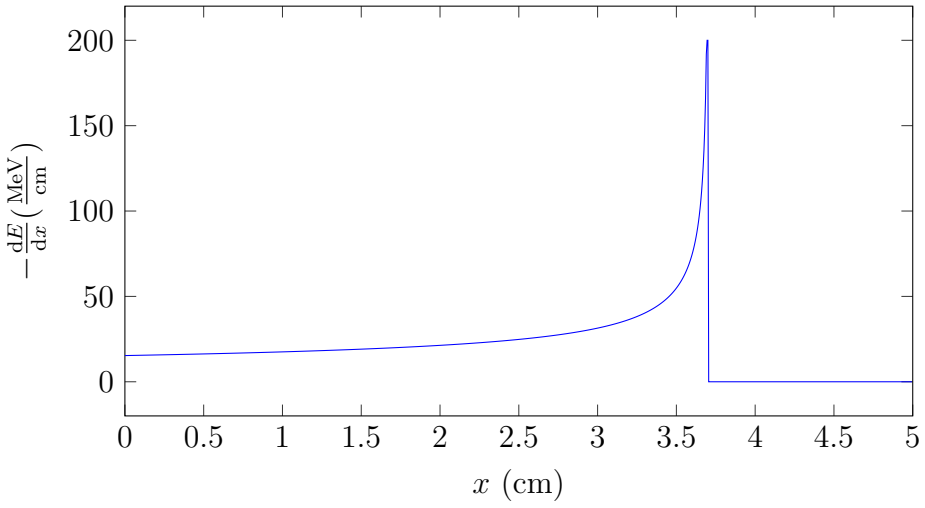

Figure 5: Theoretical Bragg curve for the stopping power of 100 Mev protons in aluminium. Calculated (i.e. numerically integrated) via Eq. 2.14 with parameters taken from literature [14].

The Bragg curve is especially of interest for radiation cancer treatment. The pronounced Bragg peak allows for a more localized energy deposition in cancerous tissue as opposed to x-rays, which loose energy via Beer's law (i.e. exponentially), and therefore affect substantially more surrounding tissue.

2.2 Energy loss fluctuations

To be more precise, the Bethe formula (Eq. 2.14) describes the average stopping power of charged particles in matter. However, when measuring single particles they substantially fluctuate around the prediction made by Eq. 2.14. In 1944 Lev Landau studied how energy loss of individual charged particles in matter is distributed [15]. The distribution he derived bears his name, and we will briefly sketch its derivation here.

Let us consider the yet unknown distribution function denoted by $f(x, \Delta)$, which describes the probability that a particle of initial energy E_0 will lose an energy amount that lies between Δ and $\Delta + \mathrm{d}\Delta$ on traversing a distance x within a given material. Furthermore, we define $w(E, \varepsilon)$ as the probability of an energy loss ε for a particle with energy E, and additionally assume that the ionization losses are small compared to the initial energy E_0, such that $w(E, \varepsilon)$ can be simplified to $w(\varepsilon)$. We may now equate the change per length $\mathrm{d}x$ of our unknown distribution function $f(x, \Delta)$ to the difference in particles that are added due to ionization losses $w(\varepsilon) \cdot f(x, \Delta - \varepsilon)\,\mathrm{d}\varepsilon$ and particles that are lost $w(\varepsilon) \cdot f(x, \Delta)\,\mathrm{d}\varepsilon$, in any given energy slice Δ, $\Delta + \mathrm{d}\Delta$. Further considering all possible ionization losses ε yields the transport equation

$$\frac{\mathrm{d}f(x, \Delta)}{\mathrm{d}x} = \int_0^\infty w(\varepsilon)\,[f(x, \Delta - \varepsilon) - f(x, \Delta)]\,\mathrm{d}\varepsilon \quad . \tag{2.17}$$

The upper limit can be set to ∞, since for ionization losses bigger than E_0 the probability is 0 (i.e. $w(\varepsilon) = 0$ for $\varepsilon > E_0$), and similarly our unknown probability function $f(x, \Delta)$ has 0 probability for negative energies (i.e. $f(x, \Delta) = 0$ for $\Delta < 0$). To find a solution to Eq. 2.17 Landau applied the Laplace transformation (an extension of the Fourier transformation) and obtained

$$f(x, \Delta) = \frac{1}{2\pi i} \int_{-i\infty+\sigma}^{+i\infty+\sigma} e^{p\Delta - x\int_0^\infty w(\varepsilon)(1-e^{-p\varepsilon})\,\mathrm{d}\varepsilon}\,\mathrm{d}p \quad . \tag{2.18}$$

Where $\sigma \in \mathbb{R}$ and $\sigma > 0$. To find an expression for the integral in the exponent of Eq. 2.18 Landau proposed the assumption that we are only interested in values of p for which

$$p\varepsilon_0 \ll 1 \quad , \quad p\varepsilon_{max} \gg 1 \quad . \tag{2.19}$$

Where ε_0 is a characteristic atomic energy (i.e. mean binding energy of the atomic electrons) and ε_{max} the maximum energy transfer (cf. Appendix A.1). We may now split the integral in the exponent of Eq. 2.18 at a certain pivot energy ε_1, that obeys $\varepsilon_1 \gg \varepsilon_0$ and $p\varepsilon_1 \ll 1$. This yields, when additionally expanding $e^{-p\varepsilon} \approx 1 - p\varepsilon$ in the first integral (as $p\varepsilon_1 \ll 1$),

$$\int_0^\infty w(\varepsilon)(1 - e^{-p\varepsilon})\,\mathrm{d}\varepsilon = p\int_0^{\varepsilon_1} \varepsilon w(\varepsilon)\,\mathrm{d}\varepsilon + \int_{\varepsilon_1}^\infty w(\varepsilon)(1 - e^{-p\varepsilon})\,\mathrm{d}\varepsilon \quad . \tag{2.20}$$

The first integral in Eq. 2.20 describes the mean stopping power up to the energy ε_1, this can thus be identified as the low momentum part of the Bethe formula (Eq. 2.14). Hence,

$$\int_0^{\varepsilon_1} \varepsilon w(\varepsilon)\,\mathrm{d}\varepsilon = \left(\frac{e^2}{4\pi\epsilon_0}\right)^2 \cdot \frac{2\pi z^2 n_e}{m_e v^2} \left[\ln\left(\frac{2\gamma^2 v^2 m_e \varepsilon_1}{I^2}\right) - \beta^2\right] \quad . \tag{2.21}$$

The second integral in Eq. 2.20 is more cumbersome to evaluate. However, when using the previous assumptions (Eq. 2.19) an approximation for $w(\varepsilon)$ can be found,[4] particularly

$$w(\varepsilon) = \left(\frac{e^2}{4\pi\epsilon_0}\right)^2 \cdot \frac{2\pi z^2 n_e}{m_e v^2} \cdot \frac{1}{\varepsilon^2} \quad . \tag{2.22}$$

Using Eq. 2.22 the second integral in Eq. 2.20 can be evaluated and yields

$$\int_{\varepsilon_1}^{\infty} \frac{1 - e^{-p\varepsilon}}{\varepsilon^2} = p\,[1 - C_E - \ln(p\varepsilon_1)] \quad . \tag{2.23}$$

Where $C_E \approx 0.5772$ is the Euler-Mascheroni constant. Plugging Eq. 2.21 and Eq. 2.23 into Eq. 2.18 and defining the variables

$$\xi = \left(\frac{e^2}{4\pi\epsilon_0}\right)^2 \cdot \frac{2\pi z^2 n_e}{m_e v^2} \cdot x \quad , \tag{2.24}$$

$$u = \xi p \quad , \tag{2.25}$$

and

$$\lambda = \frac{\Delta - \xi\left[\ln\left(\frac{2\gamma^2 v^2 m_e}{I^2} \cdot \xi\right) - \beta^2 + 1 - C_E\right]}{\xi} \quad , \tag{2.26}$$

we finally obtain the well-known expression for the **Landau distribution**

$$f(x,\Delta) = \frac{1}{\xi} \cdot \frac{1}{2\pi i} \int_{-i\infty+\sigma}^{+i\infty+\sigma} e^{u\ln u + \lambda u}\,\mathrm{d}u \quad . \tag{2.27}$$

Let us examine some properties of Eq. 2.27. λ is often expressed as $\lambda = (\Delta - \Delta_0)/\xi$. Where

$$\lambda(\Delta_0) = 0 \quad \rightarrow \quad \Delta_0 = \xi\left[\ln\left(\frac{2\gamma^2 v^2 m_e}{I^2} \cdot \xi\right) - \beta^2 + 1 - C_E\right] \quad . \tag{2.28}$$

[4] The expression for $w(\varepsilon)$ can be found by rewriting Eq. 2.7 into an integral with respect to $\mathrm{d}E$ and equating it to $\int E\,w(E)\,\mathrm{d}E = \int \frac{e^4}{(4\pi\epsilon_0)^2} \cdot \frac{2\pi z^2 n_e}{m_e v^2} \cdot \frac{\mathrm{d}E}{E}$ (ε and E are used interchangeably here).

Δ_0 can be interpreted as a parameter that shifts the position of the maximum of Eq. 2.27. While ξ on the other hand is a scale parameter and may be understood as the "broadness" of the distribution.[5]

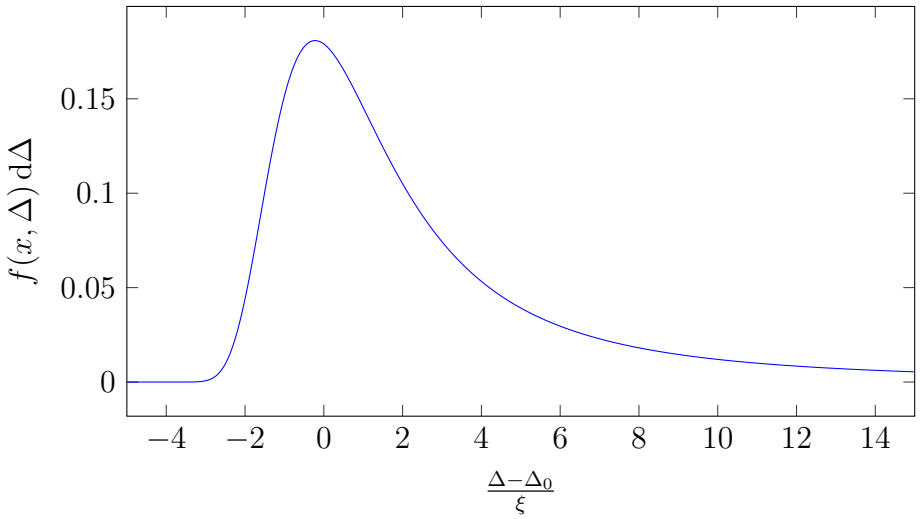

Figure 6: Plot of the Landau distribution function.

The maximum of Eq. 2.27 is at $\lambda = -0.22278$, which corresponds to the most probable energy loss (short MPV for most probable value[6]) of

$$\Delta_{mpv} = \xi \left[\ln \left(\frac{2\gamma^2 v^2 m_e}{I^2} \cdot \xi \right) - \beta^2 + 0.2 \right] \quad . \tag{2.29}$$

Finally, let us take a closer look at Landau's assumptions (Eq. 2.19) and the limitations on the applicability of Eq. 2.27 that they impose. By studying the integrand of Eq. 2.27 we may find that the contribution to the integral is by far the largest for $|u| \sim 1$. This fact together with $u = \xi p$ allows us to simplify Eq. 2.19 into

$$\xi \gg \varepsilon_0 \quad , \quad \xi \ll \varepsilon_{max} \quad . \tag{2.30}$$

The first condition of Eq. 2.30 means that the observed energies have to be sufficiently large in comparison with the atomic energies. The second condition on the other hand means that they should be sufficiently small compared to the maximum energy transfer (cf. Appendix A.1). For electrons or positrons the second condition is always fulfilled as $\varepsilon_{max} \approx E_0$ and we initially assumed that energy losses are small compared to E_0. Yet, for heavier particles the following condition must hold (cf. Appendix A.1):

$$\xi \ll 2m_e\gamma^2 v^2 \quad . \tag{2.31}$$

[5] Δ_0 and ξ are also often in analogy with the Gaussian parametrization referred to as μ and σ respectively. Yet, this analogy can be seen as quite far-fetched, as the Landau distribution's mean and standard deviation are undefined.

[6] Cern's ROOT framework oddly calls the parameter Δ_0 mpv ($\Delta_{mpv} = \Delta_0 - 0.22278 \cdot \xi$).

Landau also noted that the opposing case to Eq. 2.31, leads to a Gaussian distribution. This means that heavy particles, that loose energy too quickly or that are observed over a too long distance x, rather show Gaussian distributed fluctuations. The intermediate case can be described by the more complex Vavilov distribution [9]

$$f(\lambda;\kappa,\beta^2) = \frac{1}{2\pi i}\int_{-i\infty+\sigma}^{+i\infty+\sigma} \phi(u)\, e^{\lambda u}\,\mathrm{d}u \quad , \tag{2.32}$$

where

$$\phi(u) = e^{\kappa(1+C_E\beta^2)}\, e^{\psi(u)}, \quad \psi(u) = u\ln\kappa + (u+\beta^2\kappa)\cdot\left(\int_0^1 \frac{1-e^{-\frac{ut}{\kappa}}}{t}\,\mathrm{d}t - C_E\right) - \kappa e^{-\frac{u}{\kappa}} \quad .$$

A measure of how well the observed distribution is described by a Landau distribution is with Eq. 2.30 given by the Vavilov parameter

$$\kappa = \frac{\xi}{\varepsilon_{max}} \quad . \tag{2.33}$$

The distribution approaches a Landau distribution as $\kappa \ll 1$ (for practical purposes $\kappa \lesssim 0.01$ can be quite accurately described by a Landau distribution), whereas $\kappa \gtrsim 1$ approaches a Gaussian distribution.

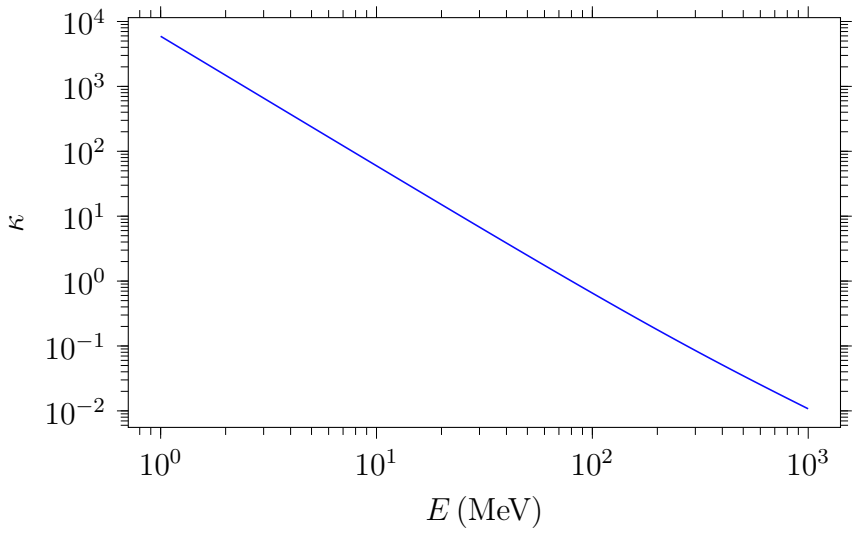

Figure 7: Vavilov parameter for different proton kinetic energies E traversing a plastic scintillator ($n_e = 3.37 \cdot 10^{29}\,\mathrm{m}^{-3}$ [14], $x = 3.2\,\mathrm{mm}$).

As a final remark, it should be noted that Eq. 2.27 can be transformed into a real integral by altering the contour line of integration (c.f. Appendix A.2). This yields the often easier to compute expression

$$f(x,\Delta) = \frac{1}{\xi}\cdot\frac{1}{\pi}\int_0^\infty e^{-u\ln u-\lambda u}\,\sin(\pi u)\,\mathrm{d}u \quad . \tag{2.34}$$

3 Experimental techniques

3.1 Scintillators

Scintillation is the production of luminescence of a material through the absorption of ionizing radiation. Luminescence on the other hand is the light emission of a characteristic spectrum. The emitted light can be categorized by its emission delay into prompt fluorescence, phosphorescence and delayed fluorescence. A material that exhibits such behaviours is known as a scintillator. Scintillators come as inorganic crystals or organic materials. The mechanisms for the production of scintillation light vary between different materials. In general, absorption leads to excitation into higher energy states, subsequent de-excitation via photon emission then produces the scintillation light. The emitted light may be absorbed again by the material, however, the emission state transition is at most of equal but often lower energy than the absorption state transition due to additional emissionless state transitions. This leads to a wavelength shift between the absorption and emission spectrum, known as the Stokes shift. For technical applications a large Stokes shift is desired to minimize self-absorption and thus increase the number of measurable photons.

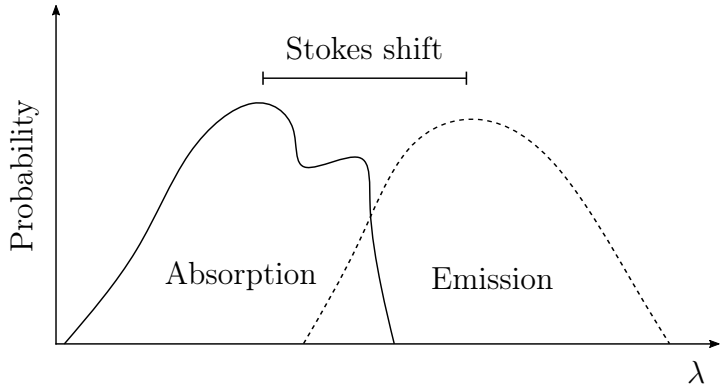

Figure 8: Schematic drawing of emission and absorption spectrum within a scintillator.

To maximize the number of photons organic scintillators often consist of three different compounds, the base scintillator, a primary additive for shorter rise times and higher quantum efficiency as well as a secondary additive that functions as a wavelength shifter and maximizes the Stokes shift.

The excitation efficiency for ionizations is generally a lot smaller ($\sim 5\,\%$) than the efficiency for direct excitation via ultraviolet photons ($\sim 50 - 90\,\%$). Yet, L the number of photons produced of a given wavelength is in good approximation proportional (by a factor S) to the energy loss of the incident particles

$$\frac{\mathrm{d}L}{\mathrm{d}x} = S\,\frac{\mathrm{d}E}{\mathrm{d}x} \quad . \tag{3.1}$$

The validity of Eq. 3.1 is only slightly limited for heavy particles with a momentum less than 100 MeV or very slow protons. Furthermore, a high number of ionization on a

given track may cause quenching effects, as the number of ionizable molecules is getting saturated. Additionally taking quenching effects into account leads to the Birks formula [16]

$$\frac{\mathrm{d}L}{\mathrm{d}x} = \frac{S\,\frac{\mathrm{d}E}{\mathrm{d}x}}{1 + \kappa_B\,\frac{\mathrm{d}E}{\mathrm{d}x}} \quad . \tag{3.2}$$

Where κ_B denotes a factor that corresponds to the strength of quenching effects. S and κ_B are determined experimentally for each scintillator via calibration, these parameters can additionally be influence by radiation damage.

The scintillation light response of organic scintillators is mostly determined by prompt fluorescence and therefore follows an exponential decay

$$I(t) = I_0\, e^{-\frac{t}{\tau_f}} \quad , \tag{3.3}$$

where τ_f is the decay constant for prompt fluorescence and I_0 the scintillation light intensity at $t = 0$. In most scintillators the much shorter rise time is negligible, for some very fast scintillators it may however be necessary to also be considered. This generally done via a constant τ_r, that describes the rise time

$$I(t) = I_0 \left(e^{-\frac{t}{\tau_f}} - e^{-\frac{t}{\tau_r}} \right) \quad . \tag{3.4}$$

In many organic scintillators also delayed fluorescence can play a role, with a larger decay constant τ_d. In such scintillators Eq. 3.3 thus becomes

$$I(t) = I_1\, e^{-\frac{t}{\tau_f}} + I_2\, e^{-\frac{t}{\tau_d}} \quad . \tag{3.5}$$

The relative strength of I_1 and I_2 largely depends on the type of radiation (p, α, n, γ).

3.2 Scintillation detectors

Scintillation detectors are among the oldest devices used to measure the via ionization losses deposited energy of ionizing particles or radiation [17]. In detail, radiation or incident particles that traverse a scintillator produce scintillation photons along their track. The photons hit a photocathode, situated at one end of the scintillator, which then emits a primary electron for each photon via the photoelectric effect. The primary electron is directed onto a series of dynodes within a photomultiplier tube, which are at increasingly higher potentials. This causes additional secondary electrons to be emitted and thus over the series of all dynodes the initial current is amplified. At the other end of the photomultiplier tube the electrons hit the anode and produce a measurable current pulse.

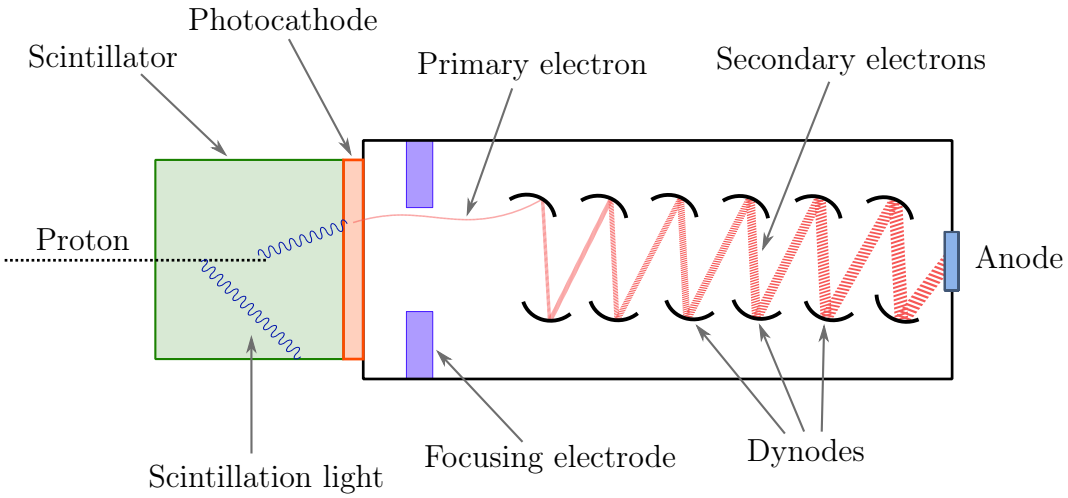

Figure 9: Schematic drawing of a scintillation detector with a photomultiplier tube.

Each of the current pulses is integrated over a time span Δt, slightly larger than the sum of rise and decay time of the scintillator and photomultiplier. Afterwards, the voltage drop along a resistor is measured. The measured voltage is proportional to the energy the incident particle or ionizing radiation lost on traversing the scintillator.

3.2.1 Silicon photomultipliers (SiPMs)

Nowadays, silicon photomultipliers are often used instead of traditional photomultiplier tubes. Even though the name suggests some similarity with a photomultiplier tube a SiPM neither contains a photocathode nor a vacuum tube, it instead consists of multiple avalanche photodiodes (APDs). An avalanche photodiode in addition to a normal photodiode contains an extra pn-junction (metallurgical junction) that further amplifies the produced electron-hole pairs via a higher intrinsic electrical field. Each avalanche photodiode operates in Geiger mode, which means that the amplification reaches a maximum and the resulting current is no longer proportional to the photon's energy (Fig. 10.

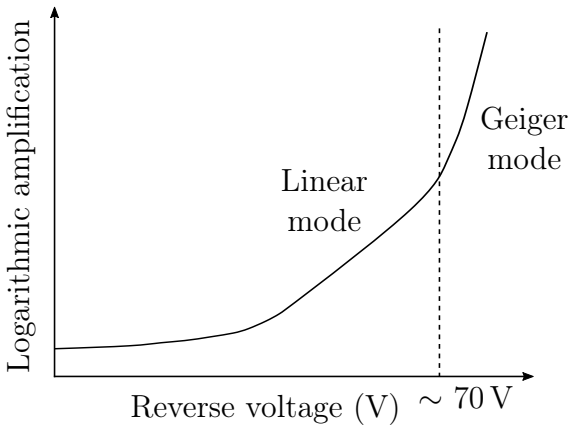

Figure 10: Schematic drawing of an avalanche photodiode's amplification.

This larger amplification is necessary to detect single photons. An SiPM contains multiple APDs arranged in a pixel grid. If the pixel size is small enough and the photons get well-

dispersed throughout the grid each photon hits a different APD cell. The probability P_{det} to detect a single photon within one such APD cell is given by

$$P_{det} = QE \cdot f_A \cdot P_G \quad . \tag{3.6}$$

Where QE is the quantum efficiency, f_A the fill factor, that describes the ratio of detection area to total area, and P_G the probability for the Geiger-process (i.e. the probability for a breakdown within the APD). If the outputs of the individual diodes are connected together, the current response is then proportional to the number of detected photons and can be measured at the SiPMS anode.

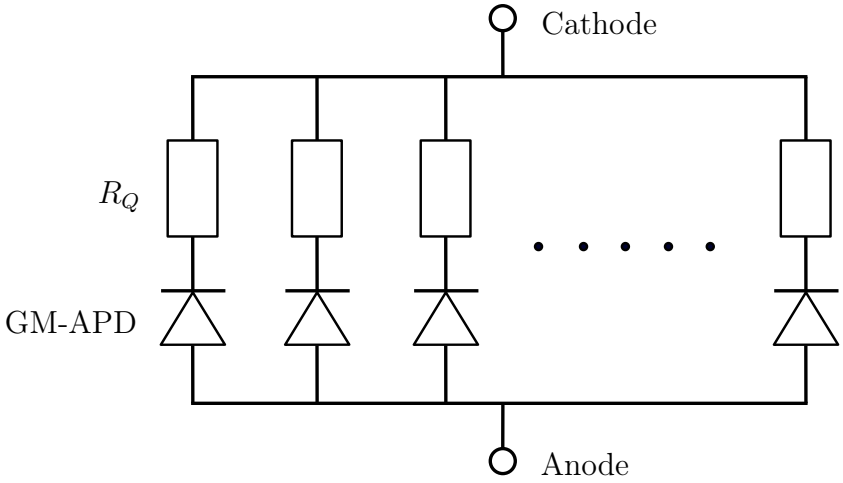

Figure 11: Equivalent circuit diagram of an SiPM.

SiPMs have a number of advantages over photomultiplier tubes, they have a higher quantum efficiency, are less sensitive to temperature and magnetic field and require substantially less bias voltage ($\sim 50 - 80\,V$), but have the drawback of a significantly larger dark current.

3.2.2 Signal fluctuations and noise

As discussed in Sect. 2.2 the ideally expected signal of a scintillation detector measuring the stopping power of individual ions shows fluctuations that follow a Vavilov distribution function, and for a small enough κ the fluctuations can be described equally well by a Landau distribution.[7] Any real measurement signal however, also contains noise from a wide range of sources.

Quantum fluctuations and Fano factor

The number of photons produced via excitations in a Scintillator naturally fluctuates according to the Poisson distribution. Yet, because the total absorbed energy has to be

[7] For our experiments at the MedAustron only the 800 MeV calibration beam can be assumed to be in the pure Landau regime ($\kappa \sim 0.015$). While the test beams ($50 - 150$ MeV) are all within the intermediate Vavilov regime. The single calibration is always in the Landau regime, since the incident particles are electrons from the beta decay of ^{90}Sr here.

dissipated somehow, there are additional restrictions on how the fluctuations can be distributed between the different radiative and non-radiative de-excitations. This causes the Poisson fluctuations $\sigma = \sqrt{\mu}$ to become

$$\sigma = \sqrt{\mu \cdot F} \quad . \tag{3.7}$$

Where F denotes the Fano factor, named after Ugo Fano.

Electronic noise
Electronic noise is the occurrence of statistical fluctuations in electronic circuits. It mainly comes from three different sources.

- **Thermal noise** is the statistical fluctuation of charges due to thermal motion. It is mostly frequency independent and thus can be considered as white noise.
- **Shot noise** is a form of quantum fluctuations within electronic circuits, diodes or photo cathodes which originates from the discreteness of electric charges.
- **1/f noise** or flicker noise summarises noise contributions with a $1/f^{\alpha}$ ($\alpha = 0.5 - 3$) spectrum. Its main source are capture and relaxation processes with different time constants.

These noise contributions result in an additional Gaussian that overlaps (or mathematically convolutes with) the measurement signal.[8]

3.3 Calorimeters for ions

Calorimeters for ions with energies low enough for negligible radiative energy losses ($E_{proton} \lesssim 100\,\mathrm{GeV}$ [12]) are generally homogeneous calorimeters, since those incident ions do not produce any particle showers.[9] They consist of a stack of scintillators (Fig. 12), where each of them is connected to a scintillation detector. Additionally, there are usually one or two scintillators that function as triggers, they notify the other scintillation detectors about an incoming ion and thus trigger a measurement. Each of the detectors then independently measures an energy

$$E_i = \int_{x_1}^{x_2} -\frac{\mathrm{d}E(x)}{\mathrm{d}x}\,\mathrm{d}x \quad , \tag{3.8}$$

that corresponds to the ion's deposited kinetic energy. Where the thickness of the scintillator is $\Delta x = x_2 - x_1$ and where E_i fluctuates according to the discussed signal fluctuations

[8] More precisely, many Gaussians for the different contributions, yet as their convolution gives a Gaussian as well they aren't separable.

[9] Unlike hadronic or electromagnetic calorimeters, which may contain a passive medium for shower development and an active one for measuring.

(Sect. 3.2.2). The signals of all scintillation detector slices are usually first digitized, then often processed by a central controller and afterwards send to a data acquisition computer.

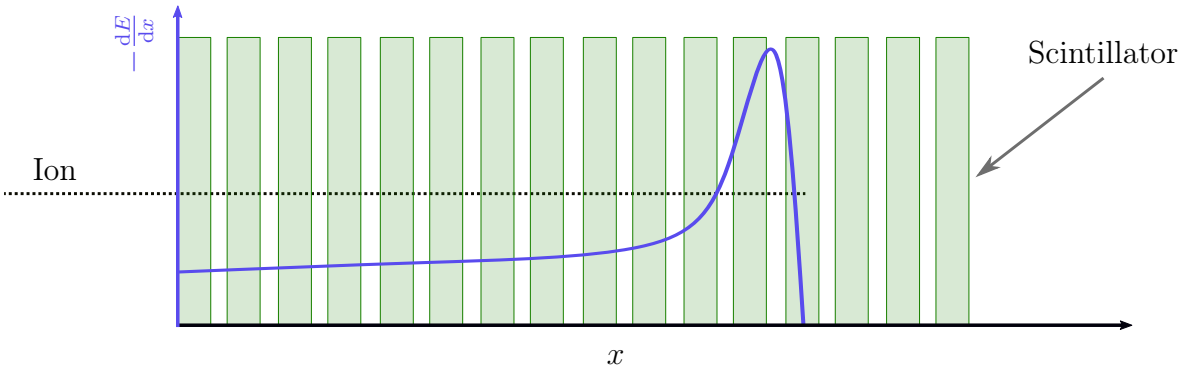

Figure 12: Schematic drawing of a calorimeter's scintillator stack.

The most important figure of merit of a calorimeter is its energy resolution

$$\frac{\sigma_E}{E} = \sqrt{\frac{a^2}{E} + \frac{b^2}{E^2} + c^2} \quad . \tag{3.9}$$

Where a summarizes the stochastic fluctuations, b the electronic or energy independent noise and c calibration errors and other irregularities. The contributions of a and c differ depending on the mode the calorimeter is operated in.

3.3.1 Sampling mode

In the sampling mode the measured energy of all scintillation detectors is summed up

$$E_{ion} = \sum_i E_i \quad , \tag{3.10}$$

to calculate the initial energy of the incident ion E_{ion}. The stochastic fluctuations a in this mode correspond to the Landau-Vavilov energy fluctuations within the individual slices. c on the other hand corresponds to the errors in the measured voltage-energy conversion or calibration factor, as well as voltage fluctuations and imprecise triggering. In this mode quenching and saturation of the scintillation detectors also contribute to b, which depending on the set-up may occur in the proximity of the Bragg peak.

3.3.2 Range telescope mode

In the range telescope mode the initial energy of the incident ion E_{ion} is inferred from the penetration depth in the calorimeter. The standard way to determine this depth or range is by identifying the last slice that measures an energy above a certain threshold. In this mode the accuracy of the individual slice's energy calibration is less important, however for a small c the materials and thicknesses of the scintillator slices have to be well known. Similarly to the sampling mode, voltage fluctuations and imprecise triggering also negatively affect the value of c. The stochastic range fluctuations a in this mode are a result of the energy fluctuations and are known under the term range straggling.

4 Material & Methods

4.1 MedAustron particle accelerator

The particle accelerator of the MedAustron was designed to accelerate protons to energies between 60 and 800 MeV and carbon nuclei to energies between 120 and 400 MeV.

By using the the distinct electron cyclotron resonance frequency $\omega_{ce} = eB/m$, the electrons of hydrogen or carbon are energized via microwaves. The energized electrons can then collide with atoms to produce ions. These ions are subsequently accelerated via a linear accelerator (LINAC), which consists of hollow tubes that are held on alternating potentials. When the ions reach the end of one tube the polarity of the tubes gets flipped to accelerate the ions to the next tube. The second acceleration stage comprises of a synchrotron accelerator with a circumference of 77 m. Here the ions are held on a circular closed-loop path by dipole magnets and are additionally focused by quadrupole magnets. The ions are accelerated via a radio frequency cavity, whose frequency is tuned up after each revolution. To keep the ions on their circular path the tune-up is synchronized with an increase in strength of the magnetic dipole field, hence the name synchrotron. Via an inhomogeneous magnetic field transversal oscillations (Betatron oscillations) are invoked in the beam. At a certain amplitude of those oscillations the ions can enter an electric septum that deflects the beam into the high energy beam transfer (HEBT). From there the ions are magnetically guided into the different irradiation rooms. [1, 18]

4.2 TERA calorimeter overview

4.2.1 Scintillation detectors

The scintillation detectors used in the TERA calorimeter consist of a plastic scintillator plate (polyvinyl-toluene) with the dimensions $30 \times 30\,\mathrm{cm}^2$ and a thickness of $\sim 3.2\,\mathrm{mm}$. The thickness was deliberately chosen for medical applications, as the range straggling in the human head plus calorimeter is expected to be $\sim 3.6\,\mathrm{mm}$ and thus there is no added benefit in using thinner plates [19]. The plates' (or slices') polished edges are connected to a cladded wavelength shifting fibre with an absorption peak at $\sim 430\,\mathrm{nm}$ and an emission peak at $\sim 495\,\mathrm{nm}$. The fibre guides the scintillation light to the silicon photomultiplier (Hamamatsu MPPC S10362-11-050C [20]). The readout electronics' PCB (printed circuit board) is mounted to one corner of the scintillator plate and has a connection to the SiPM's anode.

4.2.2 Data acquisition

The TERA calorimeter consists of 48 scintillator plates grouped into four groups (P, Q, R, S) of 12 plates. Each scintillator plate functions as a scintillation detector. Via an I^2C controllable DAC (digital to analogue converter) the over voltage ($0 - 4.97\,\mathrm{V}$) of each plate can be set, which together with the bias voltage forms the baseline voltage of the SiPM ($V = V_{bias} + V_{over}$). Each plate also contains a 12 bit ADC (analogue to digital converter) that converts the analogue signal from the SiPM into a digital one and sends it via an SPI interface to the FPGA (field programmable gate array, the programmable

low level data acquisition controller). This happens every time an external trigger (e.g. one or more trigger plates) fires.

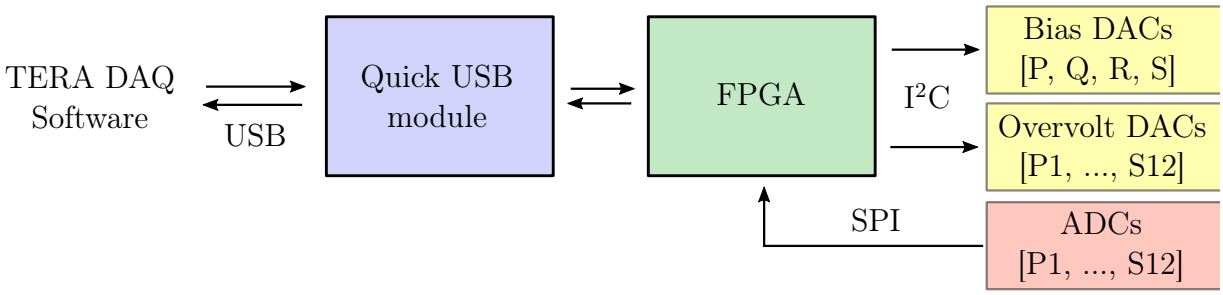

Figure 13: Schematic drawing of the data propagation within the calorimeter.

The FPGA together with the bias voltage DACs sits on the main PCB, and has a connection to each individual plate as well as the QuickUSB module [21], that is responsible for the USB connection to the data acquisition computer. The former mentioned bias voltage DACs are also controllable via the I^2C interface of the FPGA. Each bias voltage DAC thereby sets the bias voltage ($0 - 90.5\,V$) for a whole group (P, Q, R, S).

Overall, the hard- and software of the calorimeter can be summed up as setting the SiPM's baseline voltage and retrieving the raw scintillation detector signal data.

4.3 Pedestals

An artefact in the raw measurement data, that the data acquisition software has to account for, are the pedestals. These can be seen as the "true" ADC zero value or expressed differently a constant offset to every measurement produced by the readout electronics and dark current of the SiPM. The pedestals can be measured by performing a measurement without a source of incident particles.

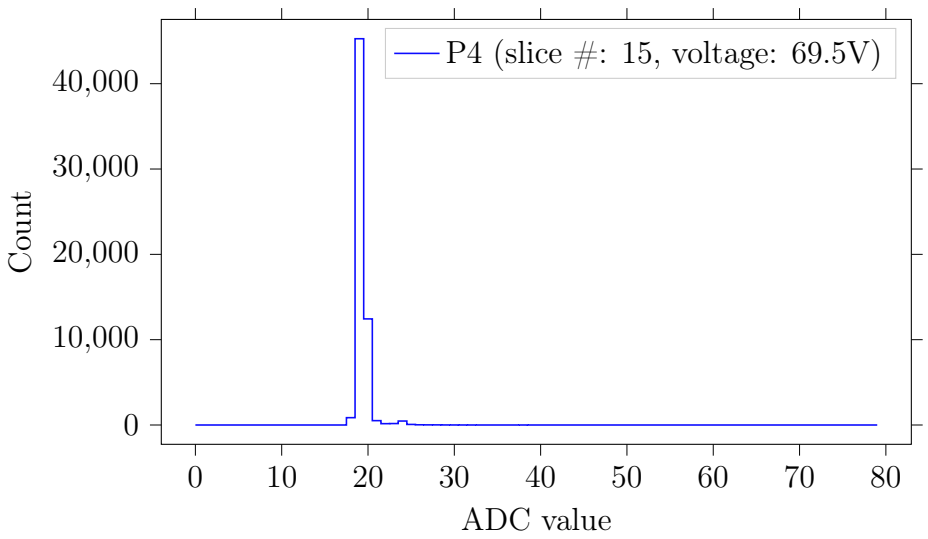

Figure 14: Plot of the histogram data for a pedestal run for scintillator plate P4 at 69.5 V.

4.4 Calibration

After determining the pedestals and accounting for them within any subsequent measurement data we may now determine the energy-ADC value conversion factor which we here denote as the calibration factor Cal, where

$$Cal = \frac{ADC_{mpv} - Pedestal}{E_{mpv}} \quad . \tag{4.1}$$

The calibration factor may be understood as the SIPM's amplification factor multiplied by the photon efficiency S (cf. Eq. 3.1) of the scintillator in units of the ADC's readout voltage steps. Determining the calibration factor was done within two different run types.

4.4.1 Single calibration

The single calibration run was performed separately for each individual plate. It was using a ^{90}Sr radioactive source together with a trigger scintillator. The trigger scintillator was connected to a photomultiplier tube which itself was connected to a trigger logic unit, that triggered events for signals over a certain threshold.

The β^--spectrum of ^{90}Sr/^{90}Y can be assumed to be reduced to the shaded region depicted in Fig. 15, since only electrons in that region have sufficient energy to make it through the plate and trigger an event. The mean energy deposition in the calorimeter's scintillator plate is almost constant for electrons between $E_{trigger}$ and E_{max}.

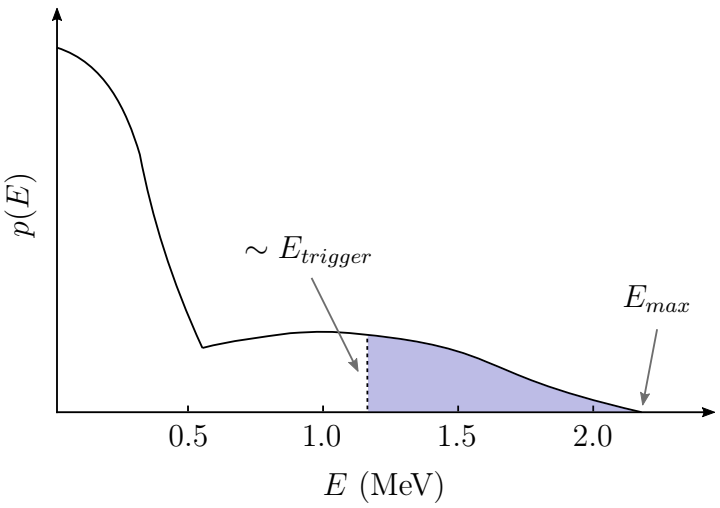

Figure 15: β^--spectrum of ^{90}Sr/^{90}Y.

The source was put in the top tray of the xy-calibration table (Fig. 16), while the trigger scintillator was put in the bottom one. The trays are moveable via four stepper motors, and we were thereby able to perform measurements at various xy-positions of the scintillator plate. This allowed us to measure the calibration factor position dependent, which may yield indications for radiation damage at certain positions and non-uniformity.

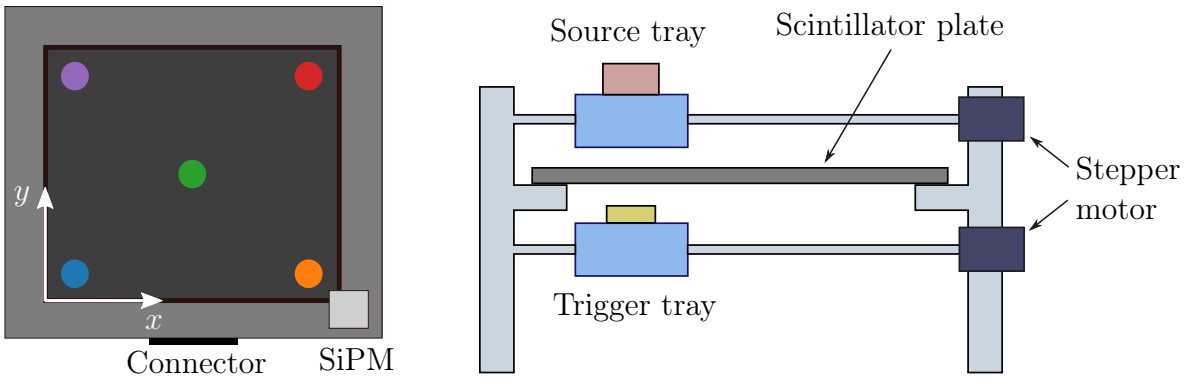

Figure 16: **Left:** Scintillator plate from the top, marked with the five different calibration positions. **Right:** Schematic drawing of the xy-table during a single calibration run.

4.4.2 Full calibration

The full calibration run was performed within the proton beam at MedAustron prior to the measurement runs. The beam energy was set to an energy (800 MeV) sufficiently high, such that the beam was able to penetrate through the whole calorimeter, which allowed all plates to be calibrated at a time. The calibration energy loss (MPV at ~ 0.6 MeV) within the individual scintillator plates was prior to the measurement determined via a Geant4 computer simulation.

4.5 Software overview

The developed software handles pedestals and calibration by associating them with different run types. A pedestal run records the pedestal values within a given voltage range and stores them in a file that can be loaded for subsequent runs. A calibration run on the other hand automatically determines the necessary voltage for each scintillation detector slice, such that the configured desired Landau MPV (c.f. Eq. 2.29) matches the measured one.[10] The also configured theoretical energy loss can then be used to determine each plate's calibration factor, which gets stored together with the voltages in a calibration result file. Once a pedestal run and a calibration run have been performed and both result files are loaded, the software is then able to automatically convert the measured ADC values, recorded in a global run, into measured energies.

The last run type, single calibration, works almost identically to the full calibration run. The only two differences are that it only calibrates one single scintillator plate and that it does the same calibration up to a specified number of times while moving the calibration table's tray to a different position in between two calibrations.

[10] In detail, this is done by adapting the voltages via an iterative approximation procedure, which is quite similar to binary search.

Figure 17: Screenshot of the main tab, that handles loading of pedestal and calibration config and result files, as well as presents the option to start the different run types.

A special emphasis was put on quick and easy quality control and debuggability by providing ways to visualize the Bragg curve (on the left side of Fig. 17) as well as the individual scintillator slices' histograms (Fig. 18). This was a necessity due to the general stability problems with the calorimeter hardware.

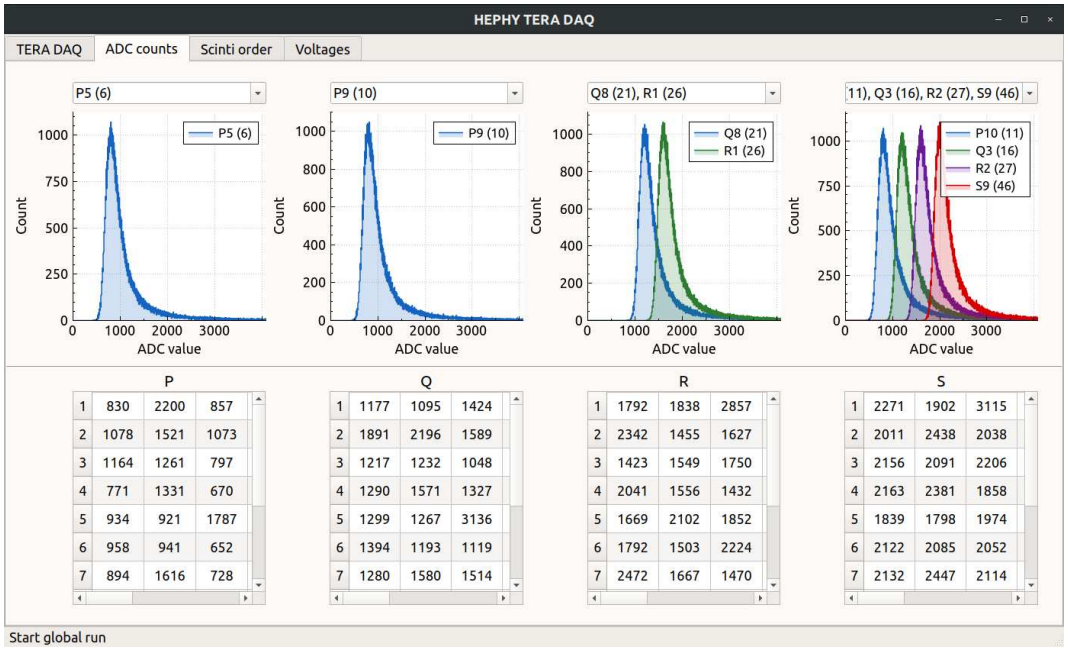

Figure 18: Screenshot of the ADC counts tab.

4.6 MedAustron measurement set-up

For our measurements at MedAustron we aligned the triggers and calorimeter such that the proton beam was passing through the centre of the triggers ($t \approx 1.4\,\text{cm}$ each) and calorimeter slices ($t \approx 3.3\,\text{mm}$ each).

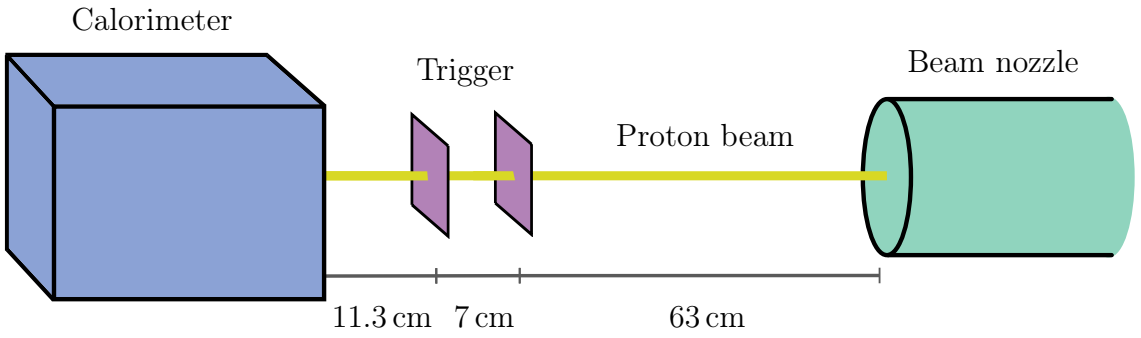

Figure 19: Schematic drawing of the measurement set-up at MedAustron with the distances between the involved instruments.

Figure 20: Photo of the measurement set-up, trigger marked with a violet rectangle and calorimeter marked with a blue rectangle. The beam's projected trajectory is indicated by the green laser.

5 Results & Discussion

5.1 Single calibration

The single calibration mostly showed a decent uniformity of the plates (Fig. 21).

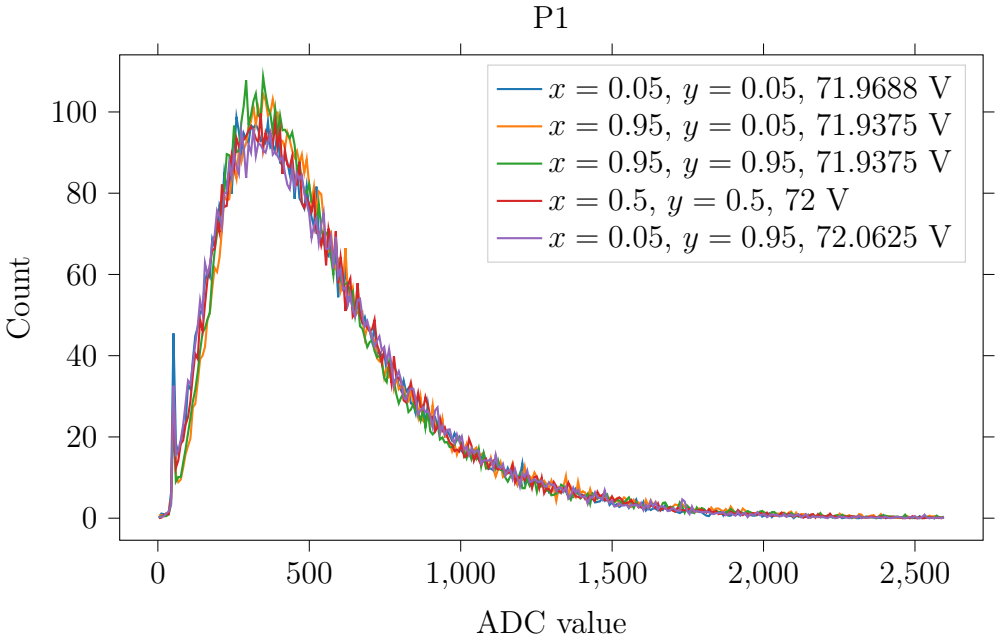

Figure 21: Single calibration histograms of a decently uniform plate at the 5 different calibration positions.

Yet, some plates like P7 and R5 ($\sim$ 9 plates in total) required a higher calibration voltage and thus exhibited a higher Gaussian sigma for the position closest to the SiPM $x = 0.95$, $y = 0.05$ (c.f. Fig. 16 for a detailed description of the positions). We believe it is unlikely that all of those scintillator plates are aligned such that the plate is always the thinnest at this position. A speculative explanation would be, that this is caused by a worse connection of the light guiding fibre to the plate in this corner, due to mechanical strain on the SiPM package during installation, transport and reordering of the plates.

R12 (Fig. 22) on the other hand likely shows a plate with a very non-uniform thickness. The voltage differences here are not as big as for the previous case, yet one can clearly observe that the right side $x = 0.95$ seems to be thicker (lower voltage) than the left side $x = 0.05$ (higher voltage). A second possible but unlikely explanation would be, that this is not caused by a difference in thickness but rather by a difference in radiation damage. This explanation is unlikely the cause, since the calorimeter was mostly irradiated in the centre [19] and thus we would expect the centre position to show the highest voltage instead.

S7 probably exhibits both phenomena, the top $y = 0.95$ seems to be thicker than the bottom $y = 0.05$, while there is likely also a bad fibre-plate connection in the corner of

the SiPM $x = 0.95$, $y = 0.05$.

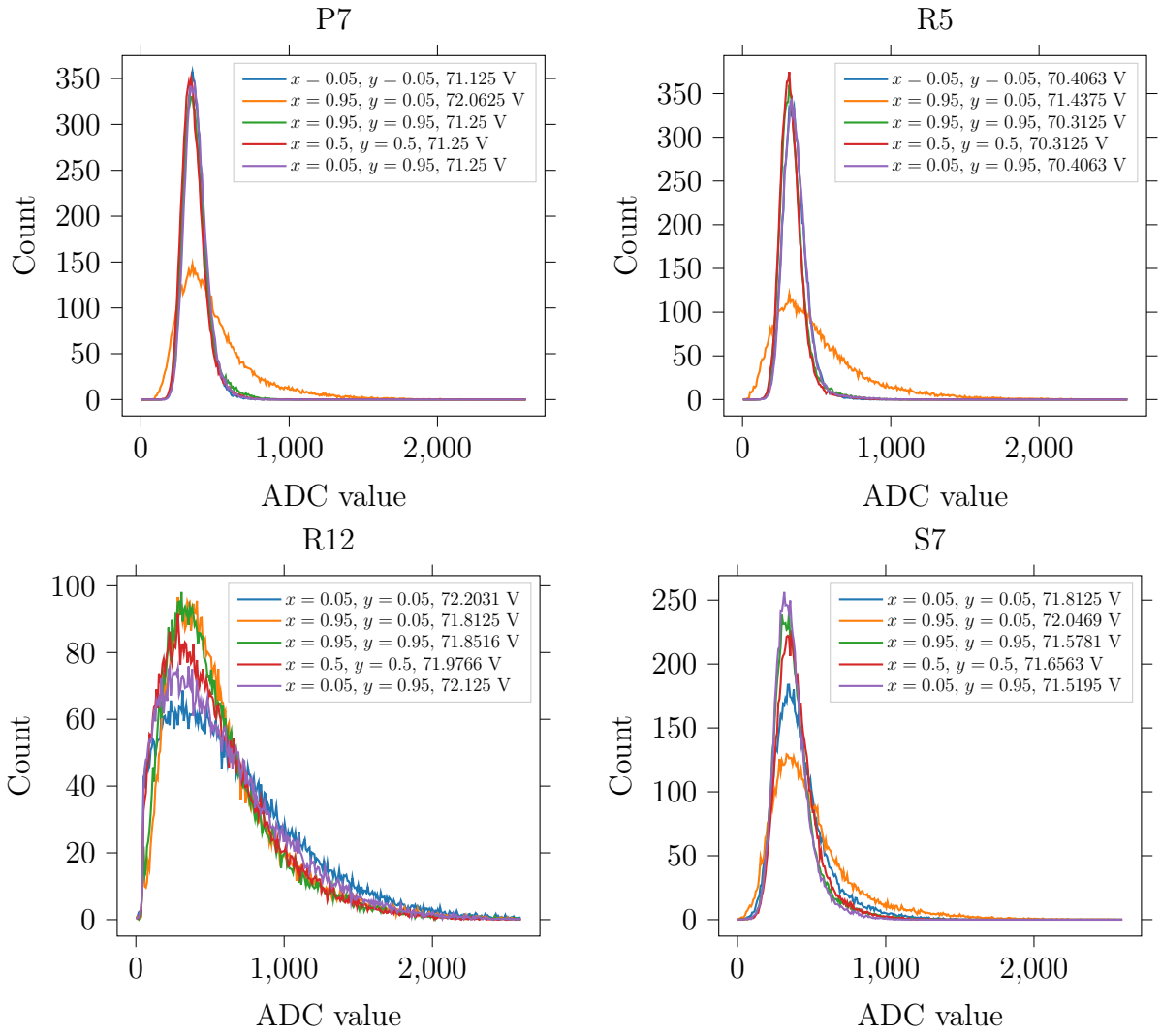

Figure 22: Single calibration histograms of 4 non-uniform slices.

The plots for all measured slices can be found in Appendix A.6.

5.2 Event rate

The calorimeter's event performance was tested prior to the measurement shift at MedAustron.

From Fig. 23 we can see that the ratio of trigger events from the TLU (trigger logic unit) to recorded events declines very quickly. At 50 kHz only about a third of the triggered events are actually recorded. While the total number of recorded events reaches a maximum at a trigger event rate of $\sim$ 50 kHz and declines slightly for higher trigger rates.

It was reported that initially the event rate was about 1 MHz [6], which we could not

reproduce, neither with the new software nor the old LabView implementation. During this study we were not able to determine the cause of this discrepancy.

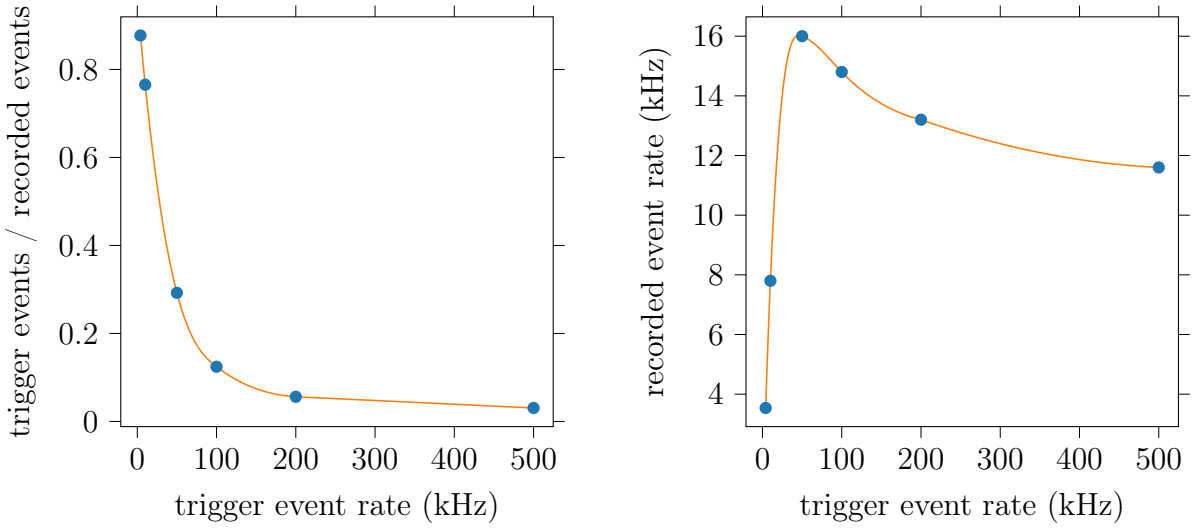

Figure 23: Event performance of the calorimeter. The orange line represents a smoothed interpolation.

5.3 Range telescope

5.3.1 Medium proton flux (∼ 400 kHz)

Calibration factor comparison

The measurements at the medium proton flux of ∼ 400 kHz were conducted with four different calibrations, each had its target MPV at a different ADC value above the pedestal. The target calibration ADC values for the MPVs were 200, 300, 400 and 600, where higher ADC values correspond to higher calibration factors (c.f. Eq. 4.1) and consequentially also higher SIPM voltages.

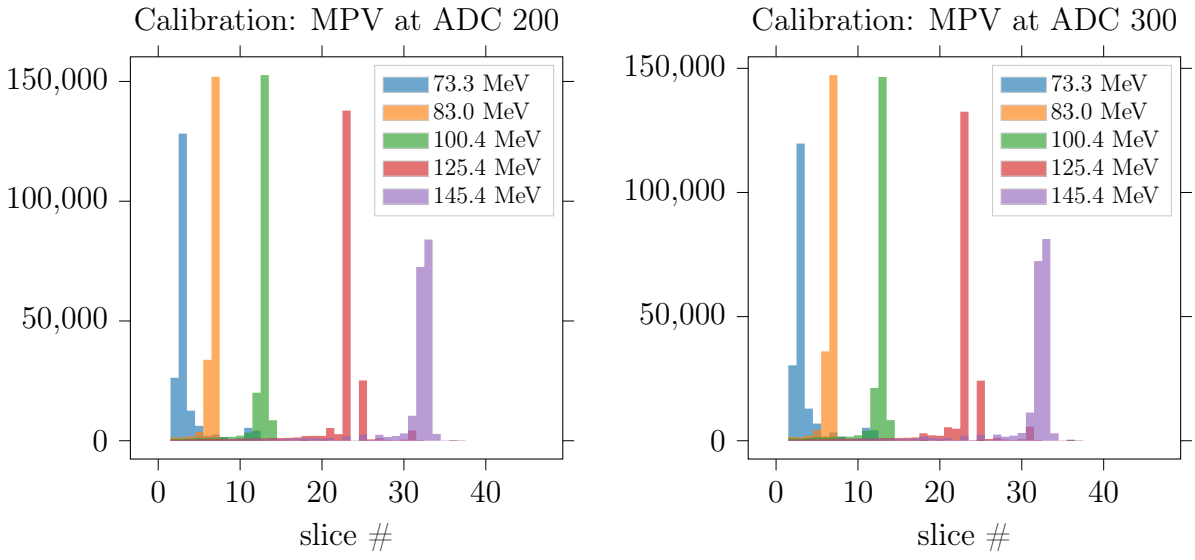

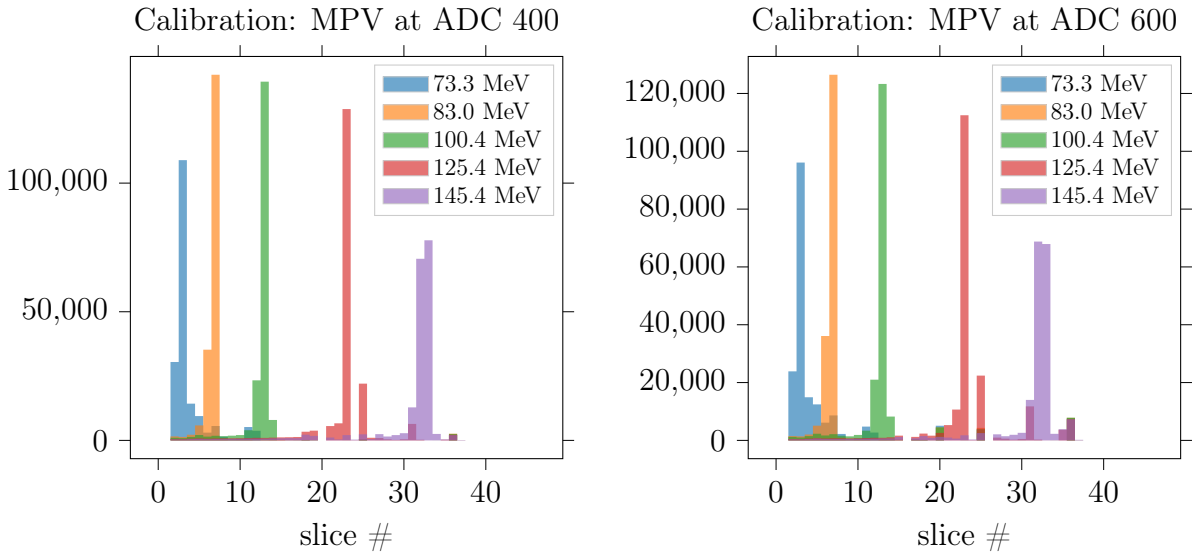

Figure 23: Last slice over 2.5 MeV histograms for different calibration factors.

A measure for how well each of the measurements is suited for single proton range determination is the sample deviation σ_s from the expected range $\overline{r}$ (c.f. Sect. 5.3.3),

$$\sigma_s = \sqrt{\frac{1}{N}\sum_{i=1}^{N}(r-\overline{r})^2} \quad . \tag{5.1}$$

This deviation corresponds to the expected error for single proton range measurements, which is notably substantially larger than the via Gaussian fitting to the histogram determined σ_G. This is due to the number and distribution of outliers in the histogram that may originate in nuclear reactions where a proton is preliminary lost, noise, bias and over-voltage fluctuations, as well as bad triggering. They only affect single particle measurements, as with enough statistics the outliers can be accurately identified as such.

From Fig. 24 we can see that the overall deviations from the expected range increase with increasing calibration factors. This is likely attributed to the higher voltage associated with higher calibration factors and the therefore induced increase in noise. This is especially noticeable for lower beam energies, which is a consequence of the last slice over threshold method that cuts off noise of preceding slices.

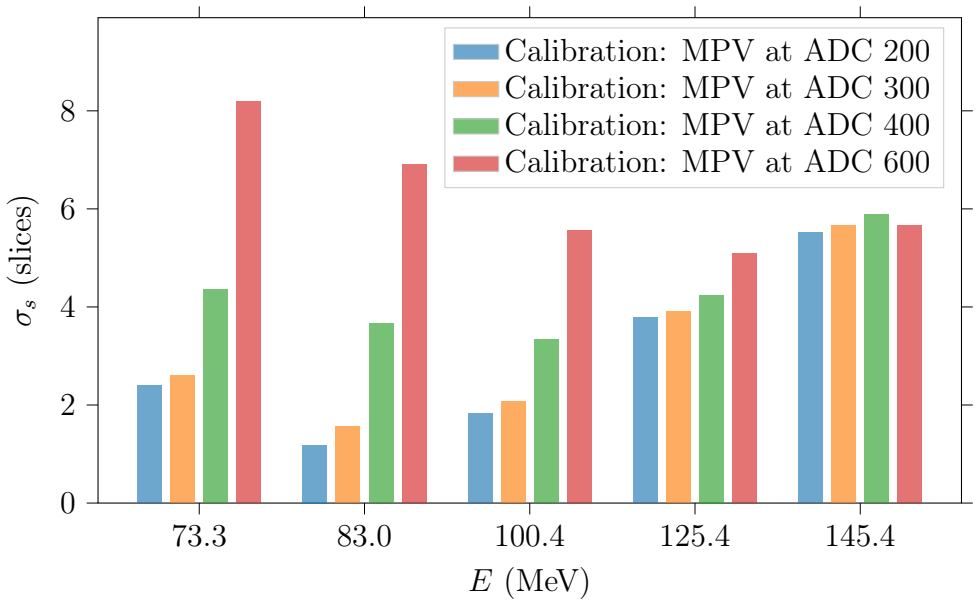

Figure 24: Comparison of different calibration factors and beam energies by their respective sample deviation from the expected range $\overline{r}$ (c.f. Sect. 5.3.3).

Bragg peak determination method comparison

The slice of the Bragg peak can be determined via a couple of different methods. We will discuss three alternatives to the standard last slice over a specific threshold method. The "first slice under a specific threshold minus one" method takes the slice right before the first slice under the specific threshold as the Bragg peak slice. It makes use of the very specific shape of energy loss fluctuations that are extending far into higher energies, yet have a distinct cut-off at lower energies (c.f. Fig. 6). A second alternative is the max signal method that uses the slice with the largest signal as the Bragg peak slice. A third proposed method is combining the "last slice over threshold" and "first slice under threshold minus one" method, such that only events where both methods agree are used.

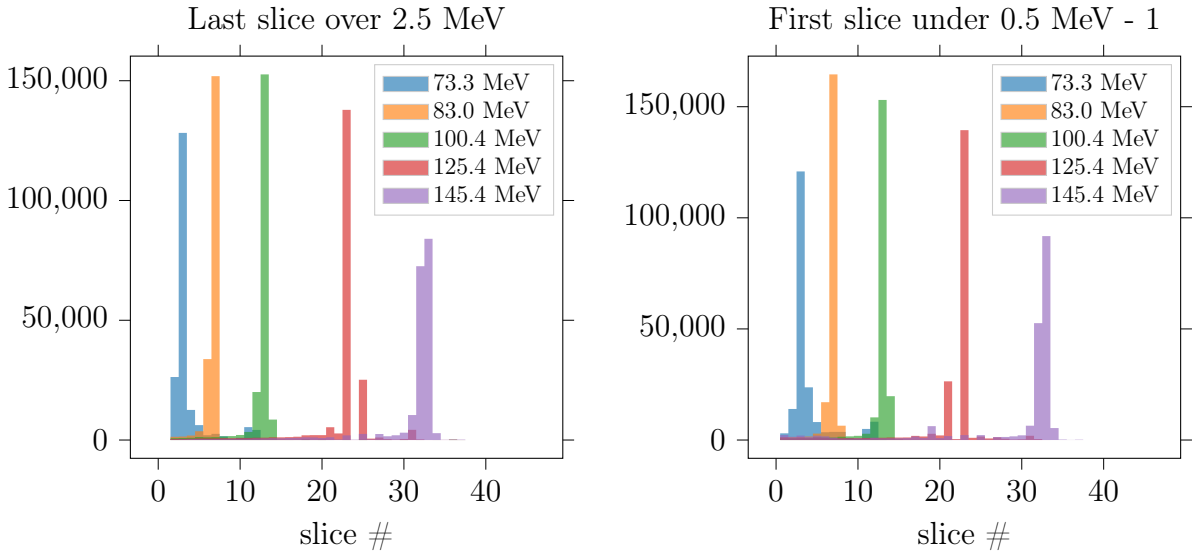

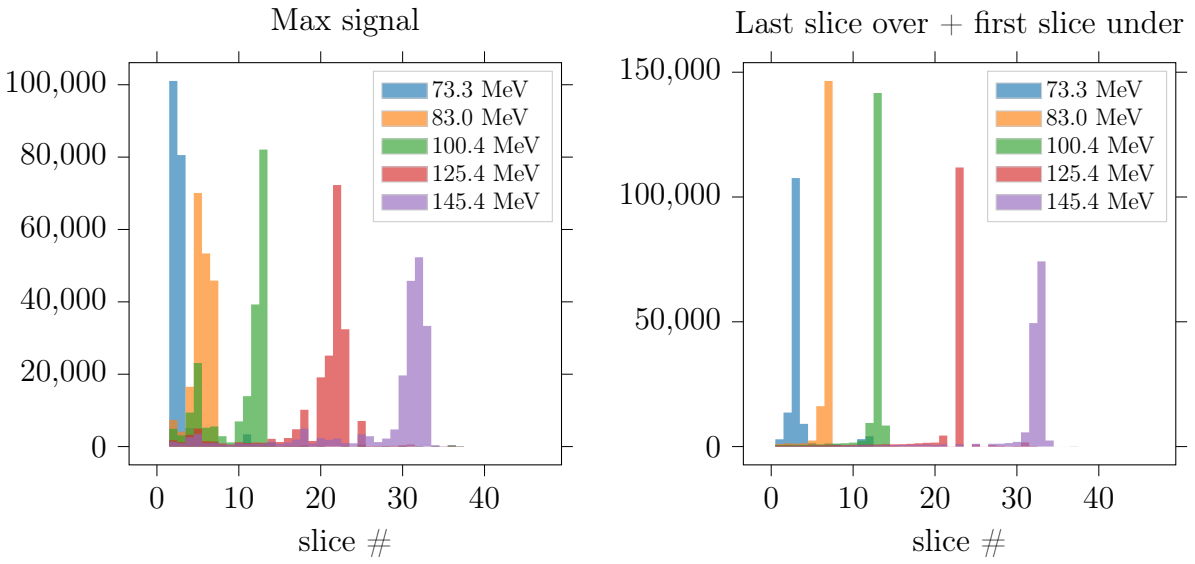

Figure 24: Bragg peak histograms for four different peak determination methods for the calibration with MPV at ADC value 200.

We can see from Fig. 24 that the last slice over threshold and first slice under threshold minus one method have very similar histograms. Yet, there is one notable difference between both. They exhibit a different noise cut-off behaviour, while the last slice over threshold cuts off more noise of preceding slices the first slice under threshold minus one method cuts off more noise of succeeding slices (very noticeable for 125.4 MeV). This fact was used to develop the combining method described earlier, which aims to combine both strengths. The max signal method is very susceptible to noise and the characteristic energy loss fluctuations and thus exhibits more spread.

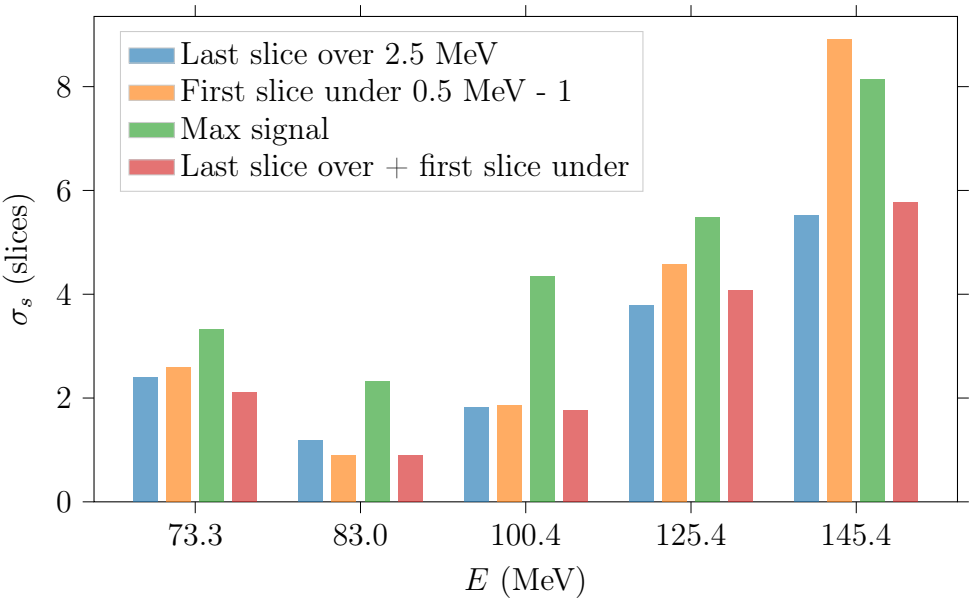

Figure 25: Comparison of different methods and beam energies by their respective sample deviation from the expected range $\overline{r}$ (c.f. Sect. 5.3.3).

Our qualitative overlook of Fig. 24 can again be quantified by the sample deviation from the expected range σ_s (Fig. 25). This reveals that indeed the combined method seems to incorporate the strengths of the last slice over threshold and first slice under threshold minus one method, showing smaller deviations at lower energies and comparable deviations to the last slice over threshold method at higher energies. The deviations for the max signal method appear to also confirm what was qualitatively said for the histograms, in that they are overall the largest for this method.

5.3.2 Low proton flux ($\sim 3\,\mathrm{kHz}$)

Earlier measurements at this proton flux have shown a second peak with a lower event count at a subsequent slice. We were thus interested in the cause of this second peak, and found that it only appeared for the low proton flux measurements. We therefore concluded that, as the beam at lower fluxes is also significantly broader in diameter that there are protons that do not pass through the triggers before entering the calorimeter. Those protons do not trigger an event themselves, but they may pile up and get picked up in a subsequent event. This can be seen when we bin the integrated recorded energy E_{total} and look at the event frequency (Fig. 26).

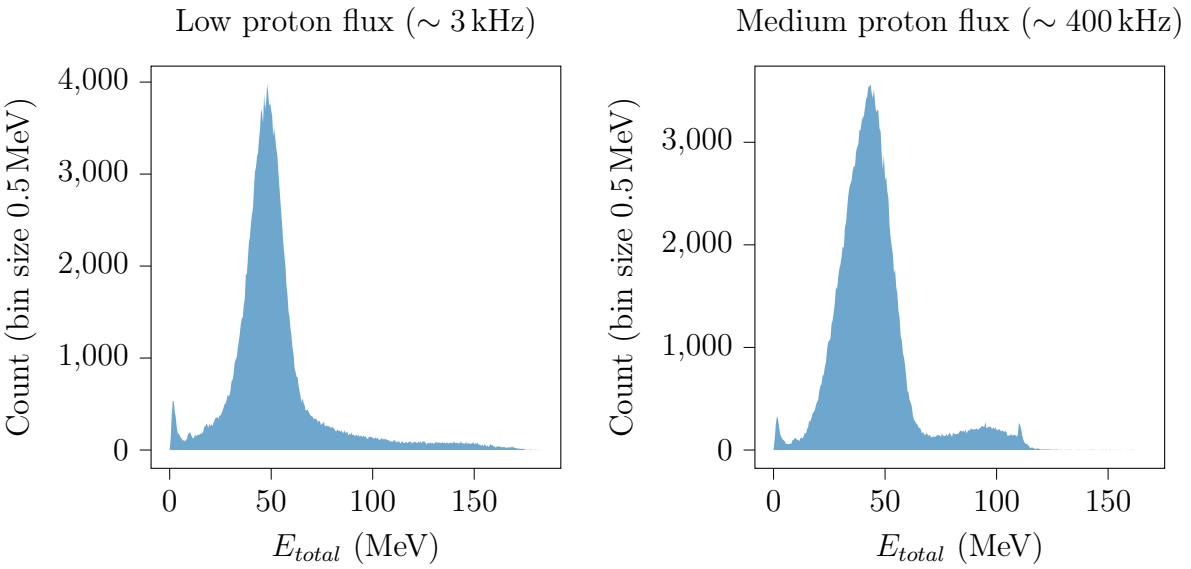

Figure 26: E_{total} frequency of the medium proton flux measurement and low proton flux measurement (Beam energy: 100.4 MeV, Calibration: MPV at ADC 300).

The high energy tail is physically impossible and thus believed to be originating in pile-up that gets added to the signal of subsequent events. It can also be noted that this pile-up is not exclusive to the low proton flux measurements.

One possible source for the pile-up is a correlated noise effect of SiPMs, afterpulsing, which is caused by charge carriers getting trapped in crystal defects and being subsequently released with a delay of several nanoseconds. They thereby induce a second avalanche in the APD cell [22, 23]. Afterpulsing was apparently a known issue in the first generation of SiPMs from Hamamatsu, which are used in the calorimeter. Later SiPM

generations were even specifically designed to minimize it [24].

Another possible source are high frequency fluctuations of the beam that result in too short time differences between two protons which then cause the signals to overlap.

Bragg peak determination method comparison

Analogously to the medium proton flux ($\sim 400\,\mathrm{kHz}$) measurements we again compared the different Bragg peak determination methods. We were mostly interested in which method could mask the second peak while also providing low deviations from the expected range.

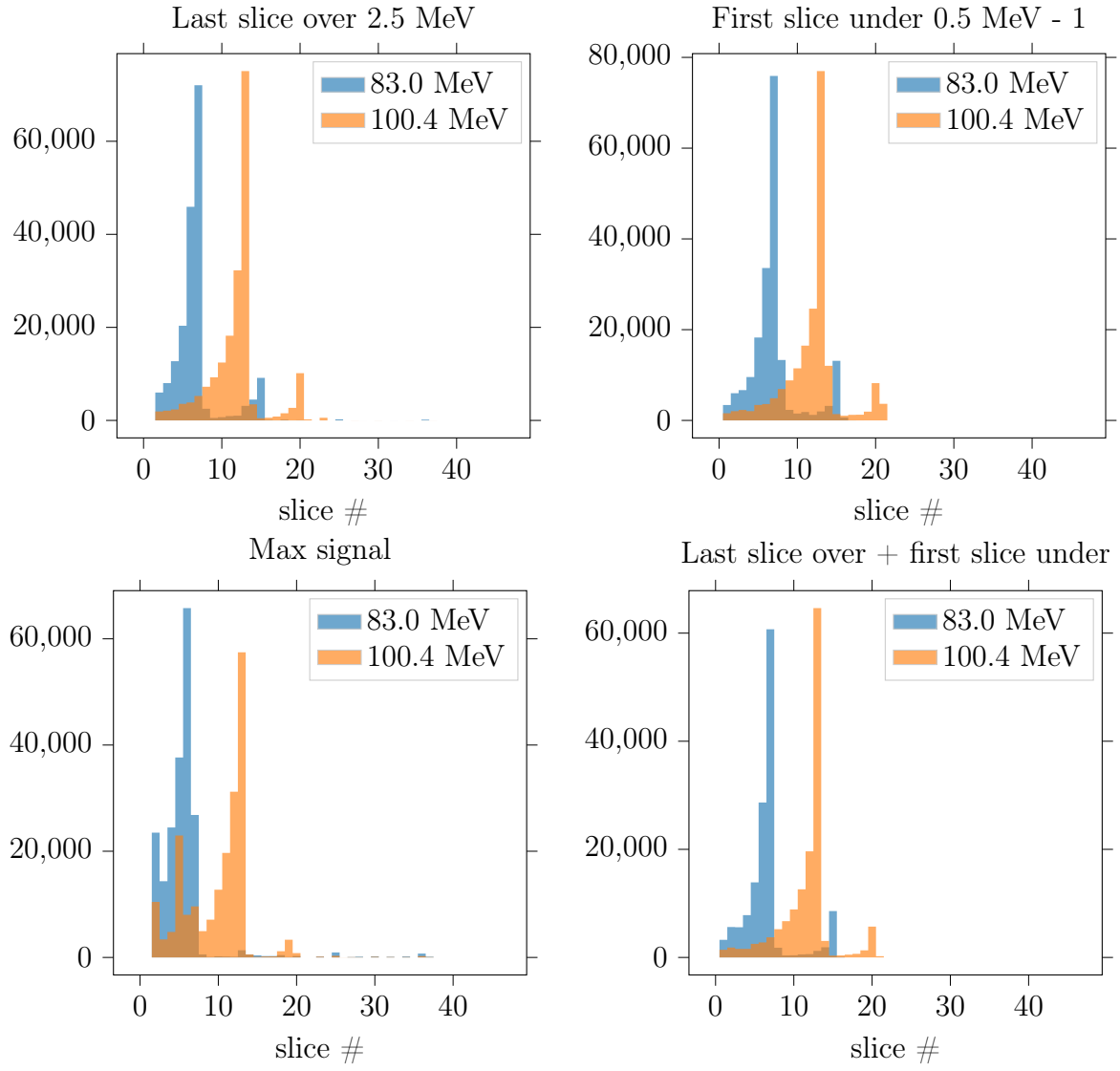

Figure 26: Bragg peak distribution histograms for four different peak determination methods for the calibration with MPV at ADC value 300.

From Fig. 26 we can observe that the max signal method suppresses the second peak best, but also comes with the previously mentioned larger spread. The other methods produce qualitatively very similar histograms.

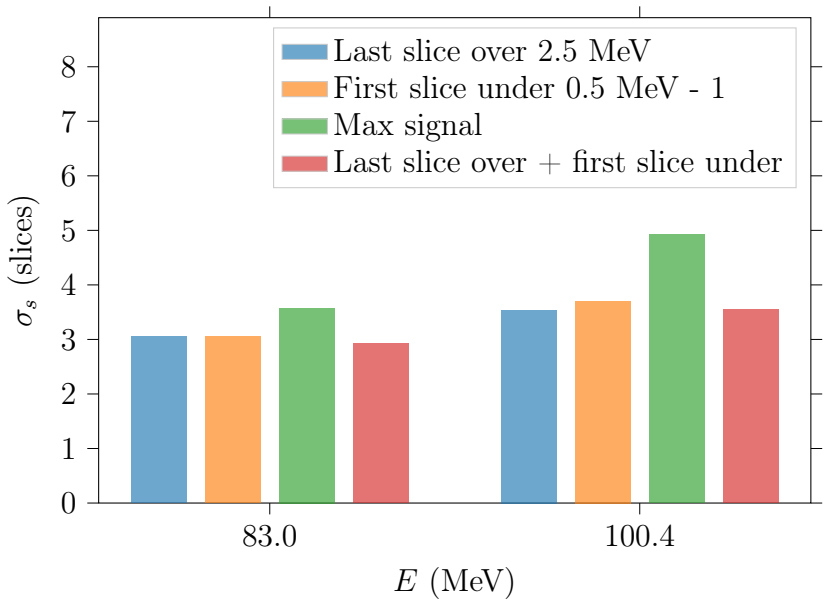

Figure 27: Comparison of different methods and beam energies by their respective sample deviation from the expected range $\overline{r}$ (c.f. Sect. 5.3.3).

The deviations from the expected range (Fig. 27) reveal that even though the max signal method suppresses the second peak, its deviations are still larger than the ones of the other methods. Overall, the deviations for the other methods are about twice as large when compared to the medium proton flux due to the second peak and possibly also because the beam has a larger angular distribution at this flux, causing larger deviations in the protons' paths.

5.3.3 Expected range

All physical ranges and thicknesses in the following section are referred to by their water equivalent range and thickness. This simplifies dealing with composite or layered materials that consist of many different base materials. The water equivalent thickness (WET) of a given material can be calculated via [25]

$$t_{WE} = t_M \cdot \frac{\rho_M}{\rho_W} \frac{\overline{S_M}}{\overline{S_W}} \quad . \tag{5.2}$$

Where $\overline{S_M}$ and $\overline{S_W}$ are the mean stopping powers of the material and water respectively. For thin targets $\overline{S}$ can be approximated by $S(E)$. If the whole energy is lost in the target the approximation $\overline{S_M}/\overline{S_W} = (\rho_W R_W)/(\rho_M R_M)$ should be used instead, where R denotes the range.

Material	Conversion (thin target at $\sim 50\,\mathrm{MeV}$)	Conversion (whole energy)
Plastic scintillator	$t_{WE} \approx t_{PS} \cdot 1.03$	$t_{WE} \approx t_{PS} \cdot 1.03$
Aluminium	$t_{WE} \approx t_{Al} \cdot 2.08$	$t_{WE} \approx t_{Al} \cdot 2.05$
PVC	$t_{WE} \approx t_{PVC} \cdot 1.14$	$t_{WE} \approx t_{PVC} \cdot 1.13$
Air	$t_{WE} \approx t_{air} \cdot 0.001$	$t_{WE} \approx t_{air} \cdot 0.001$

Table 1: A list of commonly used WET conversion factors using NIST data [14].

The mean ranges were determined via a Gaussian fit to the Bragg peak histograms of the more extensive and less error prone medium proton rate data. Furthermore, the calibration factor with an MPV at ADC value 200 was chosen together with the last slice over threshold method.

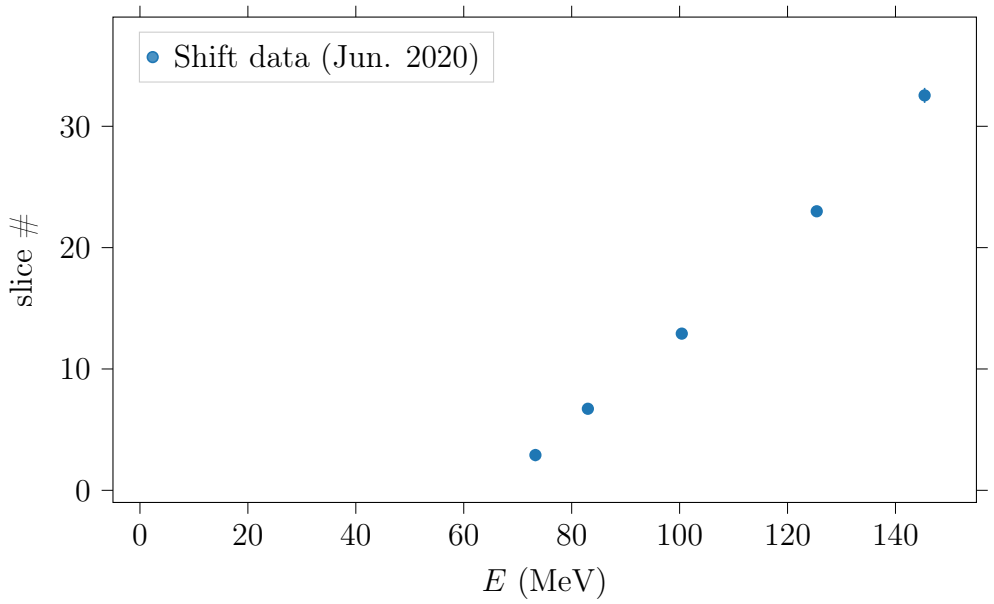

Figure 28: Gaussian fitted mean last slice over 2.5 MeV. The error bars are barely visible within the resolution of the plot.

The obtained expected ranges $\overline{r}(E)$ in calorimeter slices were then fitted to the function

$$\overline{r}(E) = \frac{R_{NIST}(E) - t_{rest}}{t_{slice}} \quad , \tag{5.3}$$

to determine the water equivalent thicknesses of the scintillator slices t_{slice} and the rest t_{rest} (trigger scintillators, wrapping, air). $R_{NIST}(E)$ here denotes the theoretical ranges for protons in water from the NIST database [14].

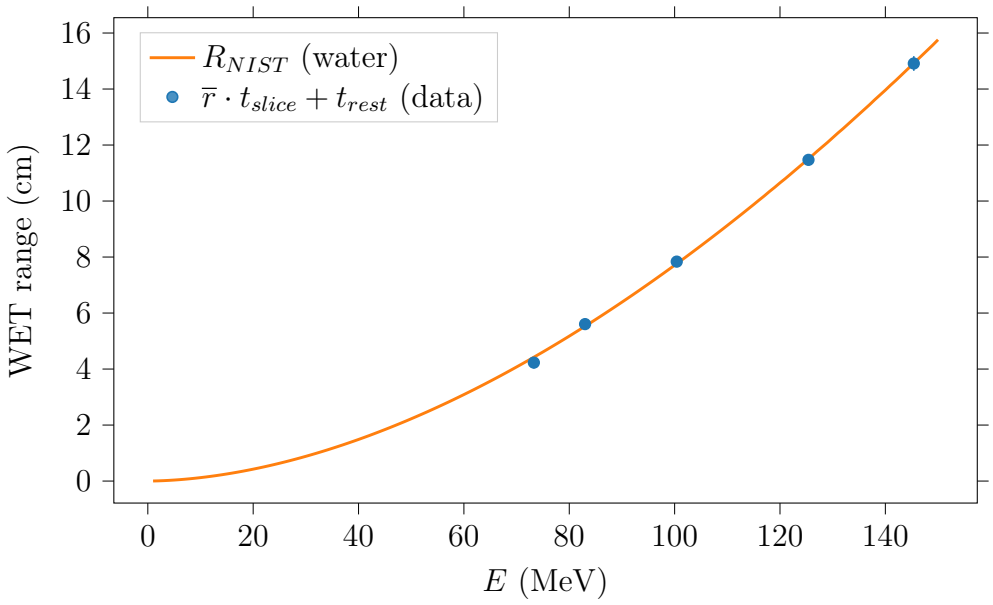

Figure 29: Comparison of the NIST water curve to the from the measurement data calculated water equivalent ranges with the obtained parameters t_{slice} and t_{rest}.

The fit yields

$$t_{slice} = 3.6 \pm 0.06\,\text{mm}, \qquad t_{rest} = 31.83 \pm 1.04\,\text{mm} \quad . \tag{5.4}$$

t_{slice} is in remarkably good accordance with the 3.3 mm WET for the 3.2 mm of plastic scintillator together with the 0.3 mm WET that were estimated for the aluminium foil and light blocking paper [19]. t_{rest} on the other hand includes the two trigger plastic scintillators, each with a thickness of 1 cm, the wrapping of those scintillators as well as the 80 cm of air between the proton beam nozzle and the calorimeter. The materials and thicknesses of the trigger scintillator wrappings could only be roughly estimated as 1 mm of aluminium foil and 7 mm of insulating tape (PVC) for both. The sum of all those contributions adds up to approximately 31.5 mm WET (cf. Tab. 1), which is also in reasonable accordance with the via fitting determined value for t_{rest}.

5.4 Sampling calorimeter

Calibration factor comparison

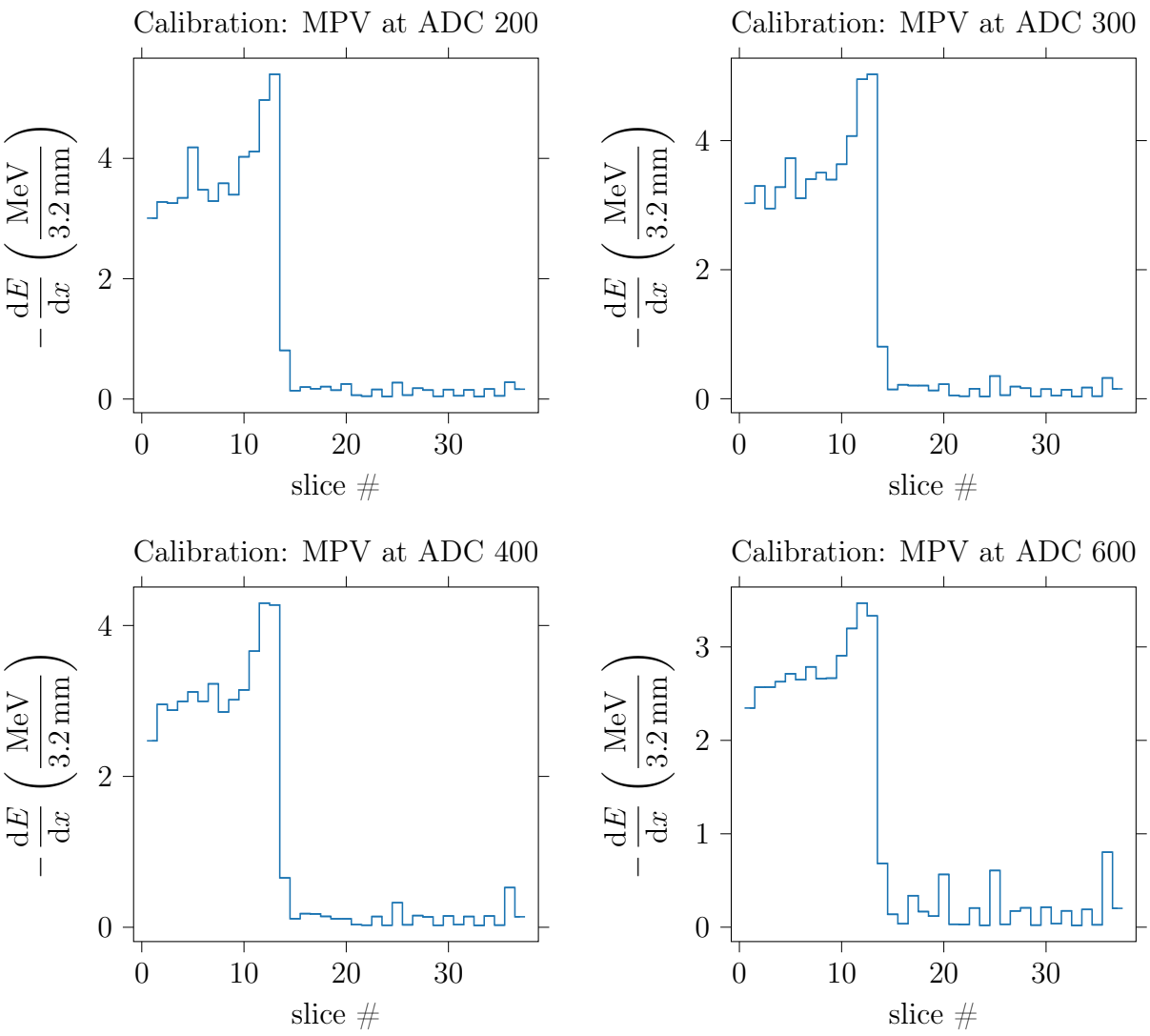

Figure 29: Mean energy loss per scintillator plate for a beam energy of 100.4 MeV (high proton rate).

From Fig. 29 we can see that lower calibration factors overall improve the resolution of the Bragg curve, which is due to the two effects. One of which is the pedestal broadening due to the higher voltage associated with a higher calibration factor. The second one is that more integration at the maximum ADC value of 4095 happens for higher calibration factors. Since 4095 is the maximum measurable value any larger voltage also gets mapped to 4095, this thus skews the calculation of the mean. The second effect is especially noticeable around the Bragg peak. From Fig. 29 one may conclude that the calibration factor should be chosen as low as possible. Yet, there is a practical limit in this direction. As the calibration factor is chosen lower and lower the separation between pedestal and the measured Vavliov energy distribution gets smaller and smaller, up to

the point at which no clear separation is possible. If this happens the resulting mean will consequently get skewed in the opposite direction. A second limiting factor in this direction is the convergence of the Landau calibration fits that need a clear separation between pedestals and the Landau energy distribution.

The fluctuations at the start of the Bragg curve are likely attributed to the non-uniform slice thicknesses, together with the fact that the calibration assumed a uniform thickness of 3.2 mm. By adding a term that describes the thickness deviation of the slices we get the true MPV energy

$$E_{mpv} = E_{cal,\,mpv} + \left.\frac{\mathrm{d}E}{\mathrm{d}x}\right|_{800\,\mathrm{MeV}} \cdot \Delta x \quad . \tag{5.5}$$

Calculating the resulting energy with the calibration energy $E_{cal,\,mpv}$ (for a calibration MPV at 200) as opposed to the true energy of the MPV E_{mpv} yields

$$E_{mes} = \frac{ADC - Pedestal}{200} \left(E_{mpv} - \left.\frac{\mathrm{d}E}{\mathrm{d}x}\right|_{800\,\mathrm{MeV}} \cdot \Delta x \right) \quad . \tag{5.6}$$

Thicker slices are thus expected to show a smaller measured energy deposition, while thinner ones are expected to show a larger energy deposition. For example, slice 5 (R9) is likely thinner than the average of 3.2 mm.

Sampling

As a sampling calorimeter the integrated measured energy up to the Bragg peak should match the total deposited energy (c.f. Sect. 3.3.1). Yet, when we compare the integrated energy (including the aluminium foil and paper) to the beam energy and also consider the supposedly 31.8 mm WET, we found to be between the beam nozzle and the calorimeter (c.f. Sect. 5.3.3), we still find a major discrepancy (Fig. 30).

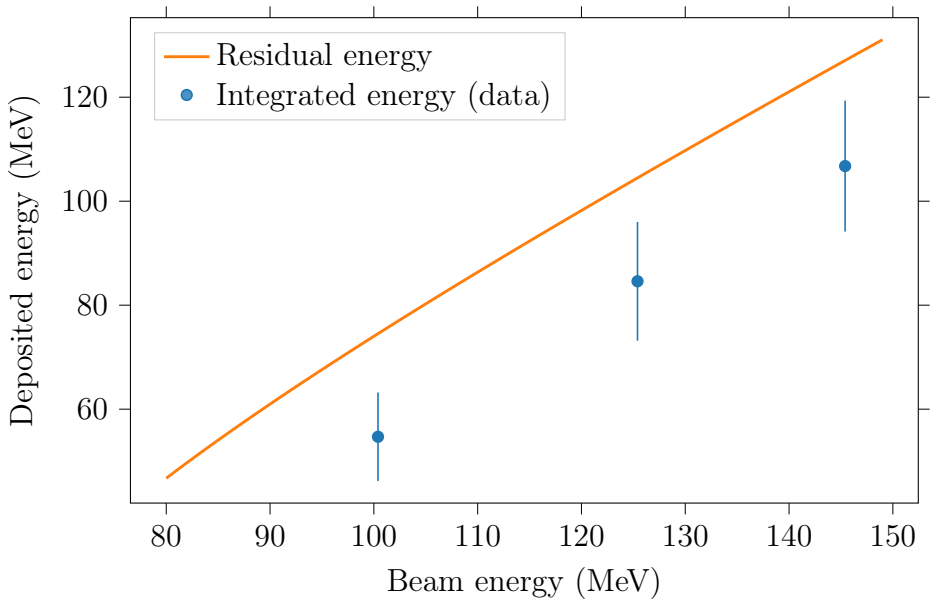

Figure 30: Integrated measured energy (including the aluminium foil and paper via a factor $t_{total}/t_{scint} = 1.09$) in comparison with the theoretical residual energy after the initial 31.8 mm WET.

This discrepancy is mostly from the slices close to the Bragg peak (Fig. 31), where scintillator quenching and SiPM saturation is expected to occur.

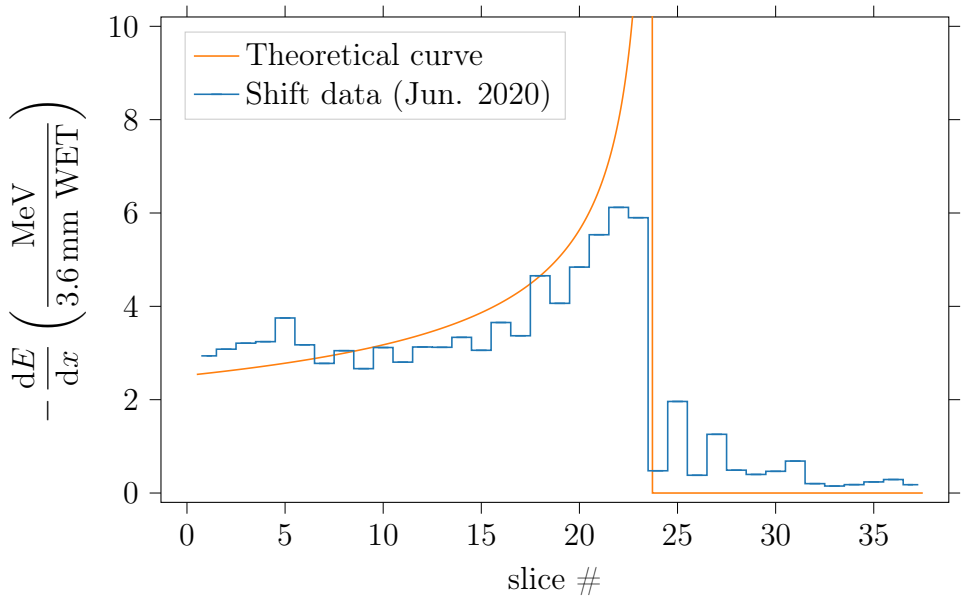

Figure 31: Comparison of the measurment data to the via the Bethe formula calculated theoretical Bragg curve ($E_{beam} = 125.4\,\mathrm{MeV}$).

The dominant effect is presumably the saturation of the SiPMs, as the used ones only contain 400 pixels and thus are only capable of measuring up to that number of photons. Any additional photons will hit already hit pixels and thereby cause pile up effects, which then result in measurement artefacts.

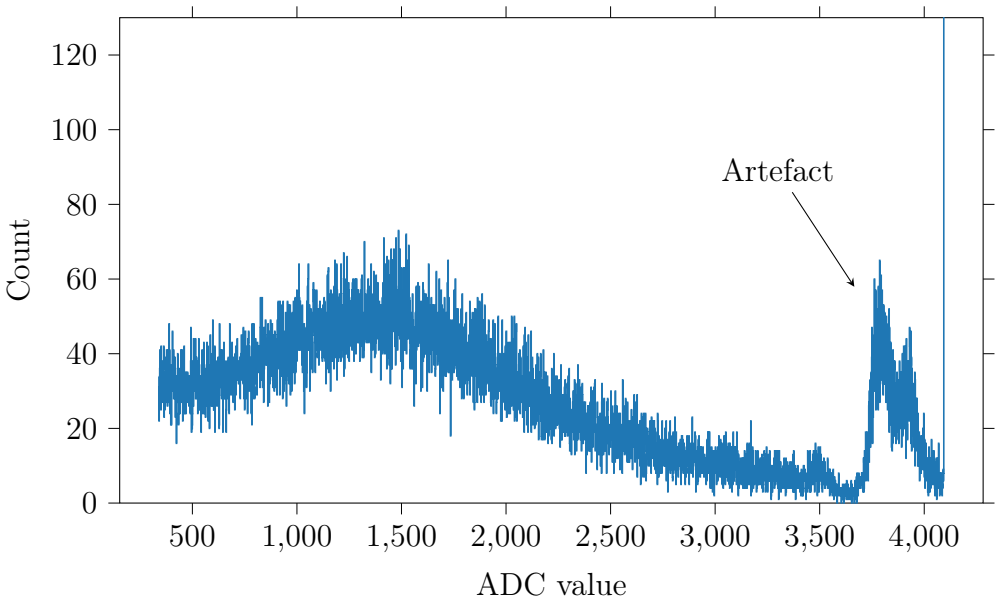

Figure 32: Histogram of a scintillator slice at the Bragg peak (145.4 MeV).

We observed a similar artefact as depicted in Fig. 32 during a pedestal measurement of a slice with a damaged light sealing. We thus strongly believe, that the depicted artefact comes from the saturation of the SiPM, as the leaked light must have saturated the SiPM during the pedestal measurement.

Furthermore, quenching and saturation additionally make computational based sampling evaluations impractical. For example, one may try to fit a Vavilov curve to the measurement data and use the obtained parameters to calculate a more precise mean energy loss per slice, circumventing the maximum ADC value limitation.

Both effects have even greater implications for single proton sampling, from Fig. 30 we can see that there is a constant offset ($\sim 25\,\mathrm{MeV}$) between the theoretical residual energy and the measured integrated energy. For a statically significant number of protons it would thus be possible to calibrate it to match the residual energies. Yet, this approach may induce a substantial error for single proton sampling, since here the specific shape of the saturation artefact is important.

Bortfeld model comparison

Starting from the empirical Bragg-Kleeman rule [26], that relates the initial beam energy E to the range

$$R(E) = \alpha E^p \quad , \tag{5.7}$$

Thomas Bortfeld developed a model [27] to describe the deposited dose profile within a material. As opposed to the Bethe formula the Bortfeld model is only valid for proton energies between 10 and 200 MeV and unlike the Bethe formula also models range straggling

and fluence reduction.[11] For a proton beam the deposited dose profile is given by

$$D(z) = \Phi_0 \frac{e^{-\zeta^2/4}\,\sigma^{1/p}\,\Gamma(1/p)}{\sqrt{2\pi}\varrho\, p\,\alpha^{1/p}\,(1+\beta R)} \cdot \left[\frac{1}{\sigma}\,\mathscr{D}_{-1/p}(-\zeta) + \left(\frac{\beta}{p} + \gamma\beta + \frac{\epsilon}{R}\right)\mathscr{D}_{-1/p-1}(-\zeta)\right] \quad , \tag{5.8}$$

with $\zeta = (R-z)/\sigma$. Where σ is the standard deviation of range straggling together with the beam energy deviation (i.e. square root of the added variances), Φ_0 the initial beam fluence, ϱ the density of the traversed material, α and p the parameters from Eq. 5.7 , β the fluence reduction slope (i.e. $\Phi(z) \propto 1 + \beta(R-z)$), γ the fraction of locally absorbed energy released by nuclear reactions, ϵ the fraction of primary fluence that contributes to the beam energy tail extending into lower energies, $\mathscr{D}$ the parabolic cylinder function and Γ the gamma function. Eq. 5.8 is thus of the form

$$D(z) = A\, e^{-\zeta^2/4}\,\sigma^{1/p} \cdot \left[\frac{1}{\sigma}\,\mathscr{D}_{-1/p}(-\zeta) + B\,\mathscr{D}_{-1/p-1}(-\zeta)\right] \quad . \tag{5.9}$$

Where A, B, σ and R can be determined via a fit to the measured mean energies per slice. For p we can use the parameter determined for water $p = 1.78$.

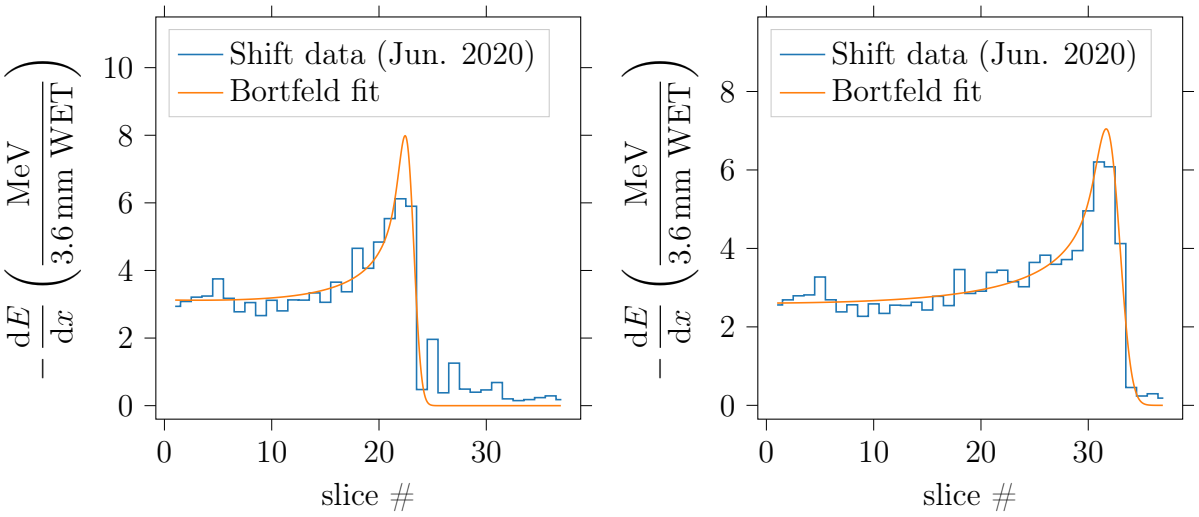

Figure 33: **Left:** Comparison of the Bortfeld fit to the measurement data at 125.4 Mev. **Right:** Comparison of the Bortfeld fit to the measurement data at 145.4 Mev.

The fits yield the parameters:

Beam energy (MeV)	A (MeV $\cdot$ cm^p)	B (1/cm)	σ (cm)	R (cm)
125.4	2.61	0.06	0.21	11.45
145.4	2.81	0.03	0.33	14.89

Table 2: Obtained fit parameters from the Bortfeld fits.

[11] **Range straggling** is the statistical deviation of the individual particles' range from the mean range. **Fluence reduction** on the other hand describes the protons that are lost from the beam due to nuclear reactions.

While σ and R are quite accurately estimated by the Bortfeld fits, the parameters A and B are very susceptible to the previously discussed sampling problems. The parameter B is expected to not change a lot with the range, as ϵ is expected to be very small for our proton beam. Yet from the fit parameters B we can calculate $\epsilon = 1.49$, which is bigger than unity and thus does not make sense physically. Similarly, one can calculate from both A parameters a negative fluence reduction β. Overall, it can thus be concluded that fitting the Bortfeld model to the calorimeter data in the current calorimeter stage can only give us a second approach for determining range straggling and the expected range (the first is a Gaussian fit to the Bragg peak histogram, c.f. Sect. 5.3.3).

Finally, it should be noted, that if we use the specific fit function Thomas Bortfeld gave for water, we find a similar inaccuracy with a substantially differing ϵ for the two measurements.

6 Conclusions

- We found no evidence for radiation damage within the scintillator plates of the TERA calorimeter.
- Currently one fourth of all usable slices appear to have a bad connection of the light guiding fibre to the scintillator in the corner of the SiPM.
- A few plates seem to have a non-uniform thickness.
- The current event rate is approximately 15 kHz, which is substantially lower than the reported 1 MHz. This discrepancy remains unclear.
- A low calibration factor is desirable for single proton range determination to minimize noise and thus deviations from the expected range.
- The overall best range determination method, in terms of deviations from the expected range, is a combination of the "last slice over threshold" and "first slice under threshold minus one" method.
- The standard "last slice over threshold" method is only slightly worse at lower ranges in the calorimeter (lower beam energies).
- The max signal method should not be used, as it overall shows the largest deviations.
- The deviation from the expected range are about twice as large for the low proton flux as for the medium proton flux. This is likely due to protons that pass by the triggers and cause correlated SiPM noise (afterpulsing), which is then picked up by subsequent events.
- The average slice thickness in the centre was found to be 3.6 mm WET, which is in good accordance with estimations for the materials.
- There seem to have been 31.8 mm WET of material between beam nozzle and calorimeter, which is also in reasonable accordance with our estimation of 31.5 mm WET for the triggers and air.
- The sampling resolution improves with lower calibration factors.
- Our data indicates saturation of the SiPMs in the proximity of the Bragg peak.
- SiPM saturation is expected to induce substantial errors for single proton sampling.
- Fitting analytical models like the Bortfeld model to the mean energy loss per slice can only accurately assess the expected range and to some degree range straggling.

7 Acknowledgement

This work was done at the Institute of High Energy Physics of the Vienna University of Technology. I would like to thank my supervisors Dipl.-Ing. Felix Ulrich-Pur and Dipl.-Ing. Dr. Thomas Bergauer for their great support, directive suggestions and instructions during this study. I would additionally like to thank Manuel Ruckerbauer and Dipl.-Ing. Alexander Burker for their help with the experiments and the MedAustron for making them possible in the first place.

Bibliography

1. M. Benedikt, A. Wrulich, *The European Physical Journal Plus* **126** (July 2011).
2. E Schnell, S Ahmad, T. D.L. F. Herman, *Medical Physics* **42**, 3368–3369 (June 2015).
3. R. Schulte *et al.*, *IEEE Transactions on Nuclear Science* **51**, 866–872 (June 2004).
4. F. Ulrich-Pur *et al.*, *Nuclear Instruments and Methods in Physics Research Section A: Accelerators, Spectrometers, Detectors and Associated Equipment* **978**, 164407 (Oct. 2020).
5. T. Li *et al.*, *Medical Physics* **33**, 699–706 (Feb. 2006).
6. M. Bucciantonio, U. Amaldi, R. Kieffer, F. Sauli, D. Watts, *Nuclear Instruments and Methods in Physics Research Section A: Accelerators, Spectrometers, Detectors and Associated Equipment* **732**, 564–567 (Dec. 2013).
7. R. Brun, F. Rademakers, *ROOT - An Object Oriented Data Analysis Framework*, `http://root.cern.ch`, 1996.
8. N. Bohr, *The London, Edinburgh, and Dublin Philosophical Magazine and Journal of Science* **25**, 10–31 (Jan. 1913).
9. H. Kolanoski, N. Wermes, *Teilchendetektoren* (Springer Berlin Heidelberg, 2016).
10. H. Bethe, *Annalen der Physik* **397**, 325–400 (1930).
11. H. Bethe, *Zeitschrift für Physik* **76**, 293–299 (May 1932).
12. D. E. Groom, S. R. Klein, *The European Physical Journal C* **15**, 163–173 (Mar. 2000).
13. P. Sigmund, *Particle Penetration and Radiation Effects* (Springer Berlin Heidelberg, 2006).
14. S. Seltzer, *Stopping-Powers and Range Tables for Electrons, Protons, and Helium Ions, NIST Standard Reference Database 124*, eng, 1993, (`http://www.nist.gov/pml/data/star/index.cfm`).
15. L. Landau, *J. Phys.(USSR)* **8**, 201–205 (1944).
16. J. B. Birks, *Proceedings of the Physical Society. Section A* **64**, 874–877 (Oct. 1951).
17. *Wikipedia: Scintillation counter*, `https://en.wikipedia.org/wiki/Scintillation_counter`.

18. F. Ulrich-Pur, *Simulation and optimization of a proton computed tomography setup at MedAustron*, Master thesis, (2018).

19. M. Bucciantonio, PhD thesis, Universität Bern, 2015.

20. *MPPC S10362-11 Datasheet*, `http://www.hamamatsu.com.cn/UserFiles/DownFile/Product/20130812155059730.pdf`.

21. *QuickUSB module, Bitwise systems*, `https://www.bitwisesys.com/index.php/products`.

22. *First Sensor: Introduction to silicon photomultipliers (SiPMs)*, `https://www.first-sensor.com/cms/upload/appnotes/AN_SiPM_Introduction_E.pdf`.

23. F. Acerbi *et al.*, *Instruments* **3**, 15 (Feb. 2019).

24. *MPPC s12572-010 Datasheet*, `https://www.hamamatsu.com/resources/pdf/ssd/s12572-010_etc_kapd1045e.pdf`.

25. R. Zhang, W. D. Newhauser, *Physics in Medicine and Biology* **54**, 1383–1395 (Feb. 2009).

26. W. H. Bragg, R. Kleeman, *The London, Edinburgh, and Dublin Philosophical Magazine and Journal of Science* **10**, 318–340 (Sept. 1905).

27. T. Bortfeld, *Medical Physics* **24**, 2024–2033 (Dec. 1997).

28. M. Bartelmann *et al.*, *Theoretische Physik* (Springer Berlin Heidelberg, 2015).

Appendix

A.1 Relativistic head on collision

We will consider two particles A and B (Fig. 34) that have prior to the collision the four-momentum

$$p_A^\mu = \left(\frac{E_A}{c}, p_A, 0, 0\right)^T, \quad p_B^\mu = (mc, 0, 0, 0)^T \quad , \tag{A.1}$$

and after the collision

$$p_{A'}^\mu = \left(\frac{E_{A'}}{c}, p_{A'}, 0, 0\right)^T, \quad p_{B'}^\mu = \left(\frac{E_{B'}}{c}, p_{B'}, 0, 0\right)^T \quad . \tag{A.2}$$

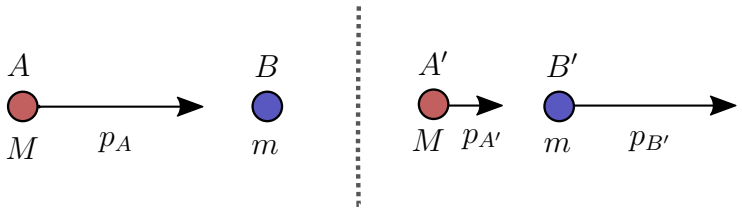

Figure 34: Schematic drawing of two particles before a head on collision (left) and after (right) in the rest frame of B.

The four-momentum of the whole system is conserved $p^\mu = p_A^\mu + p_B^\mu = p_{A'}^\mu + p_{B'}^\mu$, thus also

$$(p_A^\mu - p_{B'}^\mu)^2 = (p_{A'}^\mu - p_B^\mu)^2 \quad , \tag{A.3}$$

holds (the square here indicates multiplying by the covariant). Since $p_A^\mu p_{\mu\, A} = p_{A'}^\mu p_{\mu\, A'} = M^2c^2$ and $p_B^\mu p_{\mu\, B} = p_{B'}^\mu p_{\mu\, B'} = m^2c^2$ we can simplify this to $p_B^\mu p_{\mu\, A'} = p_{B'}^\mu p_{\mu\, A}$, which by adding $p_B^\mu p_{\mu\, B'} = p_{B'}^\mu p_{\mu\, B}$ on both sides becomes

$$p_B^\mu p_\mu = p_{B'}^\mu p_\mu \quad . \tag{A.4}$$

We will now for readability set $c = 1$ and calculate $E_{B'}$ in the rest frame of B (laboratory rest frame) by plugging Eq. A.1 and Eq. A.2 into Eq. A.4. Hence, we obtain

$$m(E_A + m) = E_{B'}(E_A + m) - p_A p_{B'} \quad . \tag{A.5}$$

Using $E_A = M\gamma$, $p_A = M\gamma v$ and $p_{B'} = \sqrt{E_{B'}^2 - m^2}$ we get after rearranging

$$E_{B'} - m = \frac{M\gamma v\sqrt{E_{B'}^2 - m^2}}{M\gamma + m} \quad . \tag{A.6}$$

Squaring both sides of Eq. A.6 and ordering by powers of $E_{B'}$ yields

$$E_{B'}^2 \left[1 - \left(\frac{M\gamma v}{M\gamma + m}\right)^2\right] - 2E_{B'}m + m^2 \left[1 + \left(\frac{M\gamma v}{M\gamma + m}\right)^2\right] = 0 \quad . \tag{A.7}$$

By solving the quadratic equation we obtain

$$E_{B'} = \frac{m \pm \sqrt{m^2 - m^2\left[1 - \left(\frac{M\gamma v}{M\gamma+m}\right)^4\right]}}{1 - \left(\frac{M\gamma v}{M\gamma+m}\right)^2} \quad . \tag{A.8}$$

Further simplifying Eq. A.8 and choosing the positive solution, as the negative one yields the trivial result $E_B = E_{B'} = m$, we subsequently find

$$E_{B'} = m\,\frac{(M\gamma + m)^2 + (M\gamma v)^2}{(M\gamma + m)^2 - (M\gamma v)^2} \quad . \tag{A.9}$$

Thus the kinetic energy gained by particle $B \to B'$ becomes after additional simplifications

$$E_{B'} - E_B = E_{B'} - m = \frac{2m\gamma^2 v^2}{1 + 2\gamma\frac{m}{M} + \left(\frac{m}{M}\right)^2} \quad . \tag{A.10}$$

A.2 Contour transformation of the Landau distribution

We will discuss the transformation of the complex Landau distribution integral

$$f(x, \Delta) = \frac{1}{\xi} \cdot \frac{1}{2\pi i} \int_{-i\infty+\sigma}^{+i\infty+\sigma} e^{u \ln u + \lambda u}\, \mathrm{d}u \quad , \tag{A.11}$$

into its real representation. We start by changing the contour line of the integration into the one depicted in Fig. 35.

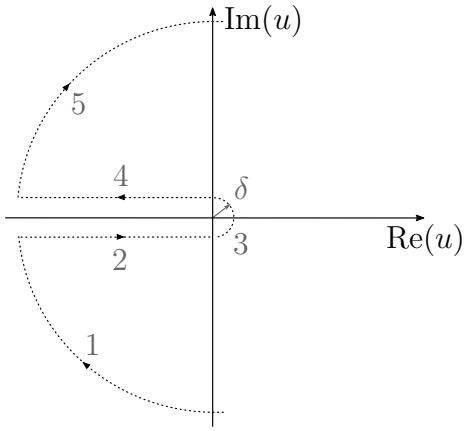

Figure 35: Drawing of the altered contour line of integration.

Cauchy's integral theorem permits us to do so, as start and end point are the same and the two contour lines don't encapsulate any singularities. We now have to evaluate the five individual integrals. Let us start with integral 1, substituting $u = r \cdot \exp(i\theta)$ yields

$$\lim_{\delta\to 0}\lim_{r\to\infty}\int_{-\frac{\pi}{2}}^{-\pi+\delta} ri\cdot e^{i\theta}\cdot e^{r[\cos\theta+i\sin\theta](\ln r+i\theta)+\lambda r(\cos\theta+i\sin\theta)}\,\mathrm{d}\theta \quad . \tag{A.12}$$

The real part of the exponent in the integrand therefore is

$$\lim_{r\to\infty} r\left[\cos\theta\cdot(\ln r+\lambda)-\sin\theta\cdot\theta\right]\to-\infty \quad . \tag{A.13}$$

One can easily see that Eq. A.13 holds for any point on the arc (for any finite λ) and thus integral 1 doesn't contribute to the overall integration value. Analogously it can be shown that integral 5 also doesn't contribute to the overall integration value. Let us now evaluate integral 3 by again reparametrizing $u = \delta \cdot \exp(i\theta)$, hence

$$\lim_{\delta\to 0}\int_{-\frac{\pi}{2}}^{\frac{\pi}{2}} \delta i\cdot e^{i\theta}\cdot e^{\delta[\cos\theta+i\sin\theta](\ln\delta+i\theta)+\lambda\delta(\cos\theta+i\sin\theta)}\,\mathrm{d}\theta \quad . \tag{A.14}$$

Here we have to evaluate the expression $\lim_{\delta\to 0}\delta\ln\delta$ in the exponent. We can do so using L'Hôpital's rule, which yields

$$\lim_{\delta\to 0}\delta\ln\delta=\lim_{\delta\to 0}\frac{(\ln\delta)'}{\left(\frac{1}{\delta}\right)'}=\lim_{\delta\to 0}-\frac{\frac{1}{\delta}}{\frac{1}{\delta^2}}=0 \quad . \tag{A.15}$$

Thus the contribution of integral 3 vanishes as $\delta \to 0$. Finally, let us take a look at the integrals 2 and 4. Hence,

$$\lim_{\delta\to 0}\frac{1}{2\pi i}\left[\int_{-\infty}^{0} e^{u(\ln|u|+i\arg(u-i\delta))+\lambda u}\,\mathrm{d}u+\int_{0}^{-\infty} e^{u(\ln|u|+i\arg(u+i\delta))+\lambda u}\,\mathrm{d}u\right]= \tag{A.16}$$

$$\lim_{\delta\to 0}\frac{1}{2\pi i}\left[\int_{0}^{-\infty} -e^{u(\ln|u|+i\arg(u-i\delta))+\lambda u}\,\mathrm{d}u+\int_{0}^{-\infty} e^{u(\ln|u|+i\arg(u+i\delta))+\lambda u}\,\mathrm{d}u\right]= \tag{A.17}$$

$$\frac{1}{2\pi i}\left[\int_{0}^{-\infty} -e^{u(\ln|u|-i\pi)+\lambda u}\,\mathrm{d}u+\int_{0}^{-\infty} e^{u(\ln|u|+i\pi)+\lambda u}\,\mathrm{d}u\right] \quad . \tag{A.18}$$

Using the identity $\sin(\pi u) = (\exp(i\pi u) - \exp(-i\pi u))/2i$ we can combine the two integrals and obtain, together with the substitution $u \to -u$, the real representation of the Landau distribution

$$f(x,\Delta)=\frac{1}{\xi}\cdot\frac{1}{\pi}\int_{0}^{\infty} e^{-u\ln u-\lambda u}\sin(\pi u)\,\mathrm{d}u \quad . \tag{A.19}$$

A.3 Outlier classification with machine learning

In Sect. 5.3 a key metric in determining the accuracy for single proton measurements, the sample deviation σ_s from the expected range was introduced. Yet, the observed deviations are still far from the physical range straggling limit due to outliers. Thus a simple convolutional network was trained on the 80 % of the measurement data for 83, 125.41 and 145.4 MeV beam energy. The remaining 20 % were used to validate the model for overfitting. The trained model was then used to filter the histogram of the untrained 100.4 MeV beam histogram (Fig. 36) to test its generalization performance.

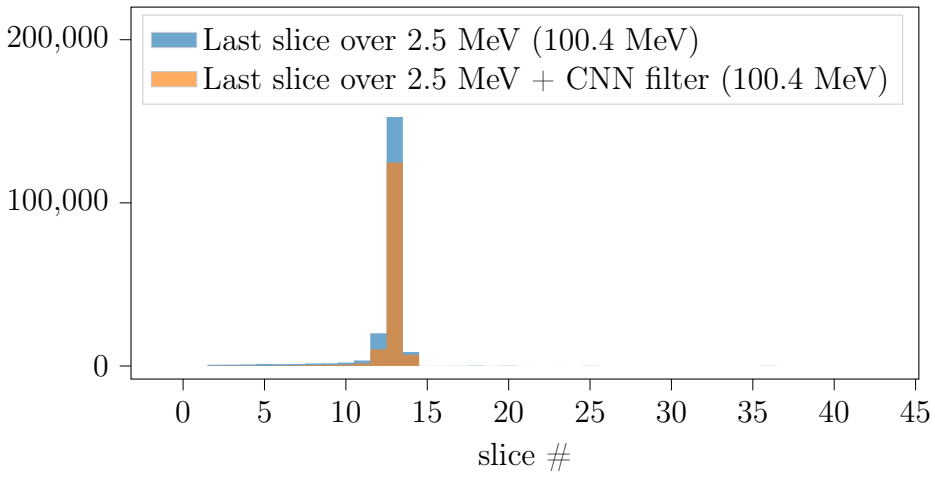

Figure 36: Comparison of the unfiltered histogram to the histogram filtered by the convolutional neural network, when generalizing from the 83, 125.41 and 145.4 MeV beam energy measurements.

Filtering decreases the deviations from the expected range from 1.8 slices to 1.0 slices. The good generalization performance indicates that this approach may indeed be used to improve the calorimeter's accuracy for measured energies between 83 and 145.4 MeV. Overall, the used model is a 1D variant of an image recognition model:

```
model = keras.Sequential([
    keras.layers.Conv1D(22, 3, activation='relu', input_shape=(len(trainEvts[0]), 1)),
    keras.layers.Dropout(0.4),
    keras.layers.MaxPooling1D(2, padding='same'),
    keras.layers.Conv1D(22, 3, activation='relu',
                        kernel_regularizer=keras.regularizers.l2(0.001)),
    keras.layers.Dropout(0.4),
    keras.layers.MaxPooling1D(2, padding='same'),
    keras.layers.Conv1D(22, 3, activation='relu',
                        kernel_regularizer=keras.regularizers.l2(0.001)),
    keras.layers.Dropout(0.4),
    keras.layers.MaxPooling1D(2, padding='same'),
    keras.layers.Conv1D(22, 3, activation='relu',
                        kernel_regularizer=keras.regularizers.l2(0.001)),
    keras.layers.Dropout(0.4),
    keras.layers.Flatten(),
    keras.layers.Dense(11, activation='relu',
                       kernel_regularizer=keras.regularizers.l2(0.001)),
    keras.layers.Dropout(0.5),
    keras.layers.Dense(1, activation='sigmoid',
                       bias_initializer=tf.keras.initializers.Constant(initial_bias))
])
```

A.4 TERA DAQ manual

The sources together with a building manual are available at `https://gitlab.com/pCT-MA/tera-daq`.

A.4.1 Main tab

Upon starting up the application the main tab will be selected and shown. It contains the Bragg curve plot views on the left and the main controls and status view on the right.

Figure 37: Screenshot of the main tab.

Status

The status view contains the logging window, which shows important messages together with the time of their occurrence. These messages are also stored in the during compile time specified "STORE_DIR" (default: the directory of the executable) within the "tera-log.txt" file. To the right of the logging window there is a combobox that lets the user choose a QuickUSB module among the connected ones. Below the combobox the most recent status message is shown, whose colour denotes the status' type.

Colour	Type
Black	Information
Orange	Warning
Red	Error

Below the status message the total number of recorded events during a run is shown.

Run control

The four yellow buttons on the right correspond to the four possible run types. The fields

above the buttons specify the data storage. Each run type produces up to three different files, they are stored in the specified storage directory and their filenames are of the form "{prefix}_{pedestal|singlecal|fullcal|global}_{datetime}{.txt.gz|_result.root|_result.txt}". Where the .txt.gz file contains the raw data, the result.root file contains the histogram data stored in a ROOT file and the result.txt file contains the specific result to the chosen run type.

Acquisition settings
Below the run control the acquisition settings are located, these are certain parameters that are important for the data acquisition of the calorimeter.

Parameter	Description	Constraints
Events per blocktransfer	Number of events that the calorimeter stores until they are transmitted to the PC	$[1, 4000]$
Max blocktransfers	Number of blocktransfer until the acquisition stops	$[1,]$
Continuous	Whether to ignore Max blocktransfers and run until the stop button is clicked	On / Off
SPI frequency	The calorimeters internal SPI frequency	Combobox values
Timeout (ms)	Time to wait between blocktransfers before the acquisition times out and stops	$[1, 2^{31} - 1]$ max ~ 23 days

Run type config and result
The configuration and result files are required and produced by the different run types respectively. They will be explained in A.4.5 and A.4.6.

A.4.2 ADC counts tab

The ADC counts tab contains tables and plot views to monitor the individual scintillator's acquired data. The top half of the tab contains four plotting views, which allow the user to select individual scintillators and plot their histograms of the current run, or if no run was started it will show the data from the last run. The plots can be zoomed by dragging a zoom window or by using the mouse wheel. There are further options within the context menu like resetting the zoom range, copying the plot to the clipboard, saving it as an image (JPG, PNG, BMP) or clearing the plotting view.

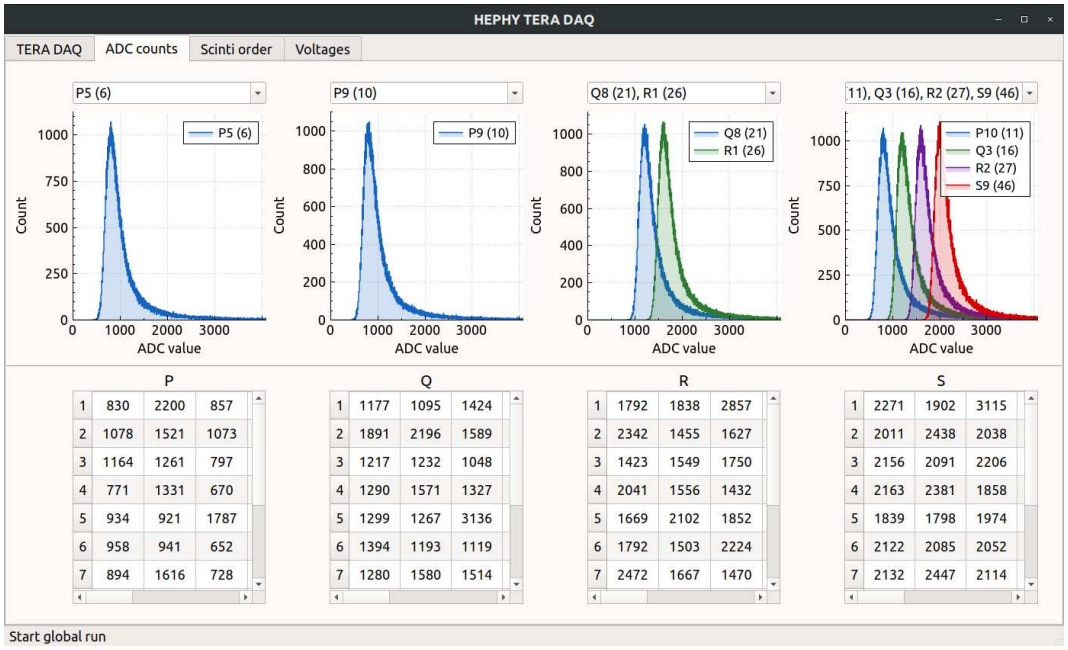

Figure 38: Screenshot of the ADC counts tab.

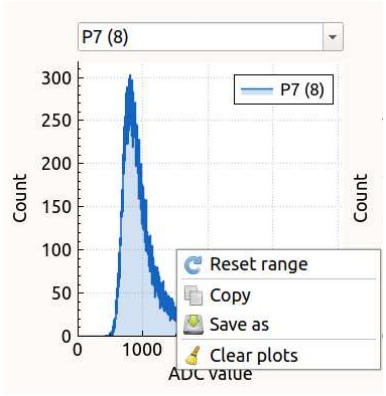

Figure 39: Screenshot of the plotting view context menu.

Below the plotting views there are four tables one for each scintillator group, that contain the latest 10 recorded events for every scintillator plate (Fig. 38).

A.4.3 Scinti order tab

Since the scintillator plates can be ordered freely in their rack and knowing their position is important for the in-beam runs (i.e. full calibration run and global run) the software has to be aware of the scintillator order. This order can be defined in the Scinti order tab.

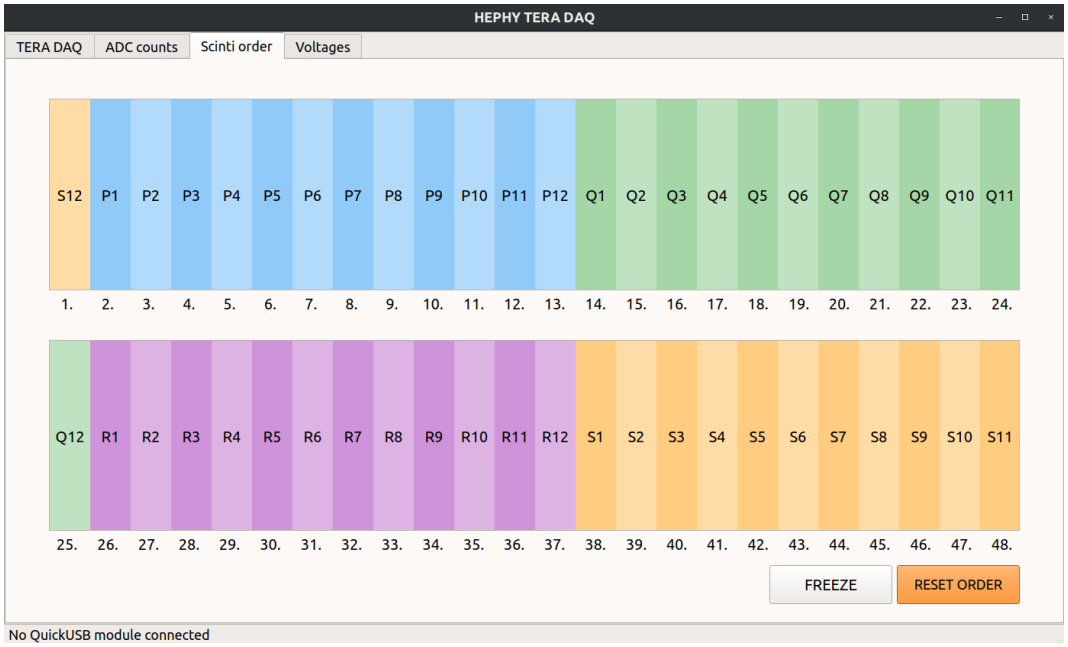

Figure 40: Screenshot of the scinti order tab.

Through drag and drop the individual scintillator plates can be moved to their global position that reflects the actual position within the rack.

A.4.4 Voltages tab

The voltages tab serves two purposes. The first one is to allow the user to slightly tweak the voltages determined during calibration. For this purpose one can use the sliders and spinboxes to change the voltages within the bias range of $[0\,\mathrm{V}, 90.5\,\mathrm{V}]$ and the overvoltage range of $[0\,\mathrm{V}, 4.97\,\mathrm{V}]$. Setting the bias voltage to OFF is equivalent to setting the voltage to $0\,\mathrm{V}$. The BIAS ON / OFF switch generally (i.e. for all groups) controls whether there is any bias voltage applied. The SAVE and LOAD buttons allow the user to save overvoltages to a file and load them again from one respectively. It should be noted that instead of setting the voltages within this tab, in most cases they should be loaded from a calibration result file and applied via the blue reapply button, located on the main tab.

The second purpose of the voltages tab is to monitor the voltages during a run. This may be important for pedestal and calibration runs, as both of those alter the applied voltages after each step.

A.4.5 Pedestal run

To start a pedestal run you should first create a pedestal configuration file. One such file can be found within the tera-daq source's /conf directory. The following configurations have to be set within the pedestal config file:

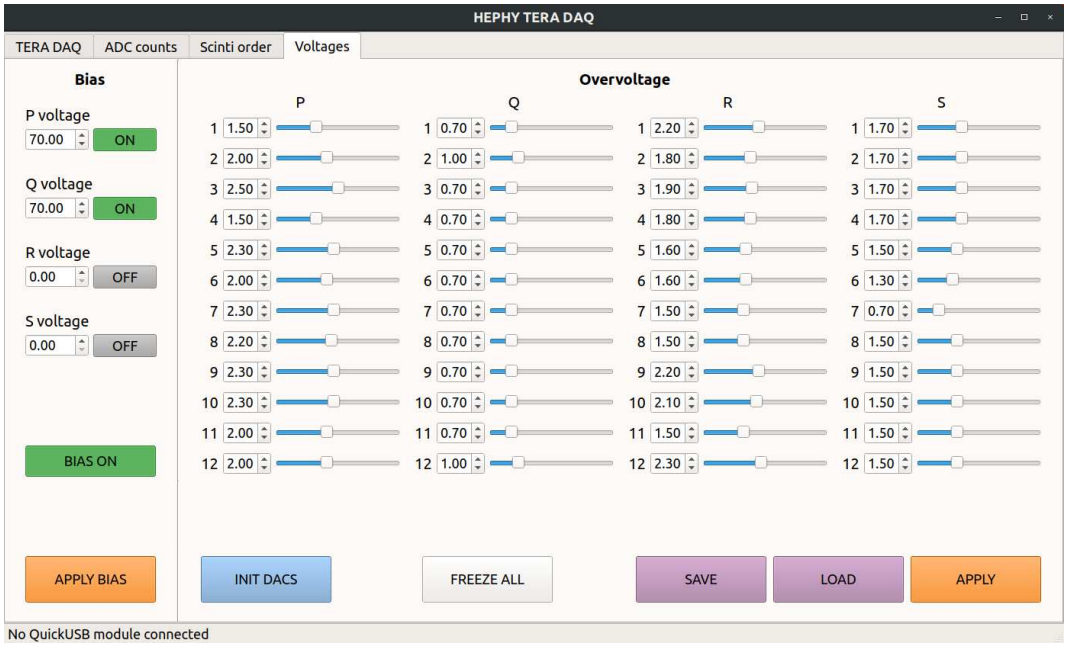

Figure 41: Screenshot of the voltages tab.

Config key prefix	Config key suffix	Description
PEDESTAL_MIN_V_	[P,Q,R,S]	Minimum or start voltage for pedestal sweep (inclusive)
PEDESTAL_MAX_V_	[P,Q,R,S]	Maximum or end voltage for pedestal sweep (inclusive)
PEDESTAL_STEP_V_	[P,Q,R,S]	Voltage step

This file has to be then loaded from the main tab before starting the pedestal run.

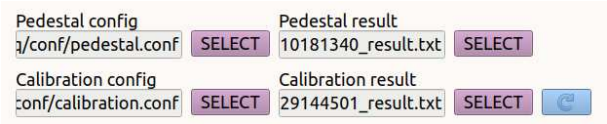

Figure 42: Screenshot of the main tab's config / result file section.

Each pedestal run will create a _result.txt file containing the results of the pedestal run. This includes for each voltage and scintillator the mean, max and median ADC value together with RMS and standard deviation as well as the fit parameters of a Gaussian fit to the pedestal data.

A.4.6 Calibration run

To start a calibration run a recent pedestal _result.txt file must be loaded as well as a calibration config file. A calibration config file can also be found within the tera-daq source's /conf directory. The following configurations have to be set within this file:

Config key prefix	Config key suffix	Description
CAL_MAX_STEPS	-	Maximum number of steps until the calibration fails if it hasn't converged yet
CAL_EPSILON_ADC_MPV	-	MPV tolerance ±
CAL_FINAL_FIT_STEP	-	1 = do a final step with the already found voltages and calculate calibration factors from it
CAL_MIN_V_	[P,Q,R,S]	Lower calibration voltage limit
CAL_MAX_V_	[P,Q,R,S]	Upper calibration voltage limit
CAL_ADC_MPV_	[P1, ..., S12]	Desired ADC value from the pedestal that should reflect the MPV of the calibration LanGaus curve
CAL_E_	[P1, ..., S12]	Energy of the MPV
CAL_TABLE_X_	[1, 2, ...]	X position(s) for the single calibration run
CAL_TABLE_Y_	[1, 2, ...]	Y position(s) for the single calibration run

Note: By only specifying a subset of all scintillator plates' CAL_ADC_MPV_ and CAL_E_ configurations, it is possible to exclude the not configured plates from the calibration run.

In detail, the calibration will start at $(V_{max}+V_{min})/2$, depending on whether the measured MPV is above or below the desired ADC value $(V_{max}-V_{min})/2^{n+1}$ (n = step number) will be subtracted or added until the MPV is reached within the set MPV tolerance.

A calibration run will create a calibration _result.txt file that contains the final LanGaus fit parameters, the calibration voltage and calibration factor for each successfully calibrated scintillator. This file may then be loaded from the main tab. Via the blue reapply calibration button the calibration voltages can then be applied.

Single calibration
The single calibration run will additionally show a dialogue when selected, in which the scintillator plate to calibrate, as well as a file name for the coalesced calibration data has to be specified. This coalesced calibration data file is equivalent to the _result.txt file of the full calibration run. Furthermore, the shown dialogue also allows the user to move the trays of the xy table to the zero position by using the keyboard arrow keys.

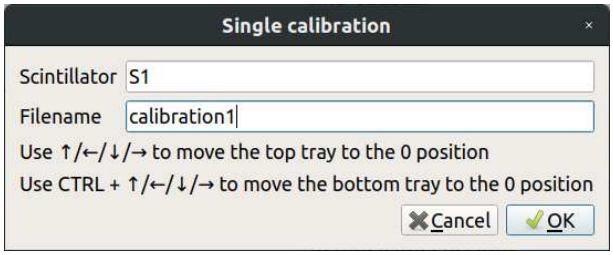

Figure 43: Screenshot of the single calibration dialogue.

A.4.7 Global run

Before starting a global run a pedestal _result.txt file should be loaded as well as a calibration _result.txt file. Furthermore, the calibration voltages should be manually applied via the blue reapply button before starting the run.

A.4.8 Data file format

The **.txt.gz** files contain the raw ADC measurement data. Every run within these files contains the following header:

```
# Order:  P1,P2,..
# Voltages (V): P1=70.0,P2=72.0,...
#
#Scinti ADC value Event number
```

After the header each line corresponds to a plate's measured ADC value together with the trigger event number in the order:

```
P1 {P1 ADC} {P1 event number}
Q1 {Q1 ADC} {Q1 event number}
R1 {R1 ADC} {R1 event number}
S1 {S1 ADC} {S1 event number}
P2 {P2 ADC} {P2 event number}
Q2 {Q2 ADC} {Q2 event number}
...
R12 {R12 ADC} {R12 event number}
S12 {S12 ADC} {S12 event number}
P1 {P1 ADC} {P1 event number}
Q1 {Q1 ADC} {Q1 event number}
...
```

Additionally, the file may contain extra comment lines prefixed by a #.

The **_result.root** files contain the histograms for each run in a CERN ROOT file format.

The **_energies.root** are only generated for calibrated global runs and contain two trees named "GlobalSliceOrder" and "CaloEvents". The "GlobalSliceOrder" tree contains branches that function as a map of [1-48] → [P1, ..., S12] that describe the global order. The "CaloEvents" tree contains 48 branches [P1, ..., S12] and an extra branch for the trigger number ("TriggerNr"). Each of the scintillator branches contains an array of the recorded energies of that scintillator slice while the trigger number branch contains the recorded event numbers.

A.4.9 EUDAQ2 integration

A building, installation and technical overview manual can be found in the eudaq directory of the tera-daq repository. The TeraProducer links the main tera-daq GUI program to EUDAQ2. The initialize step thereby just opens the tera-daq GUI and establishes a connection, while the configuration step sets all necessary configurations. This includes GUI configurations and pedestal and calibration configurations. The configuration step additionally specifies the run type that will be started on DoStartRun(). Note: Pedestal and calibration result files are still loaded by the tera-daq GUI program and thus the configuration step only specifies the location of those result files.

A.5 Pedestal data

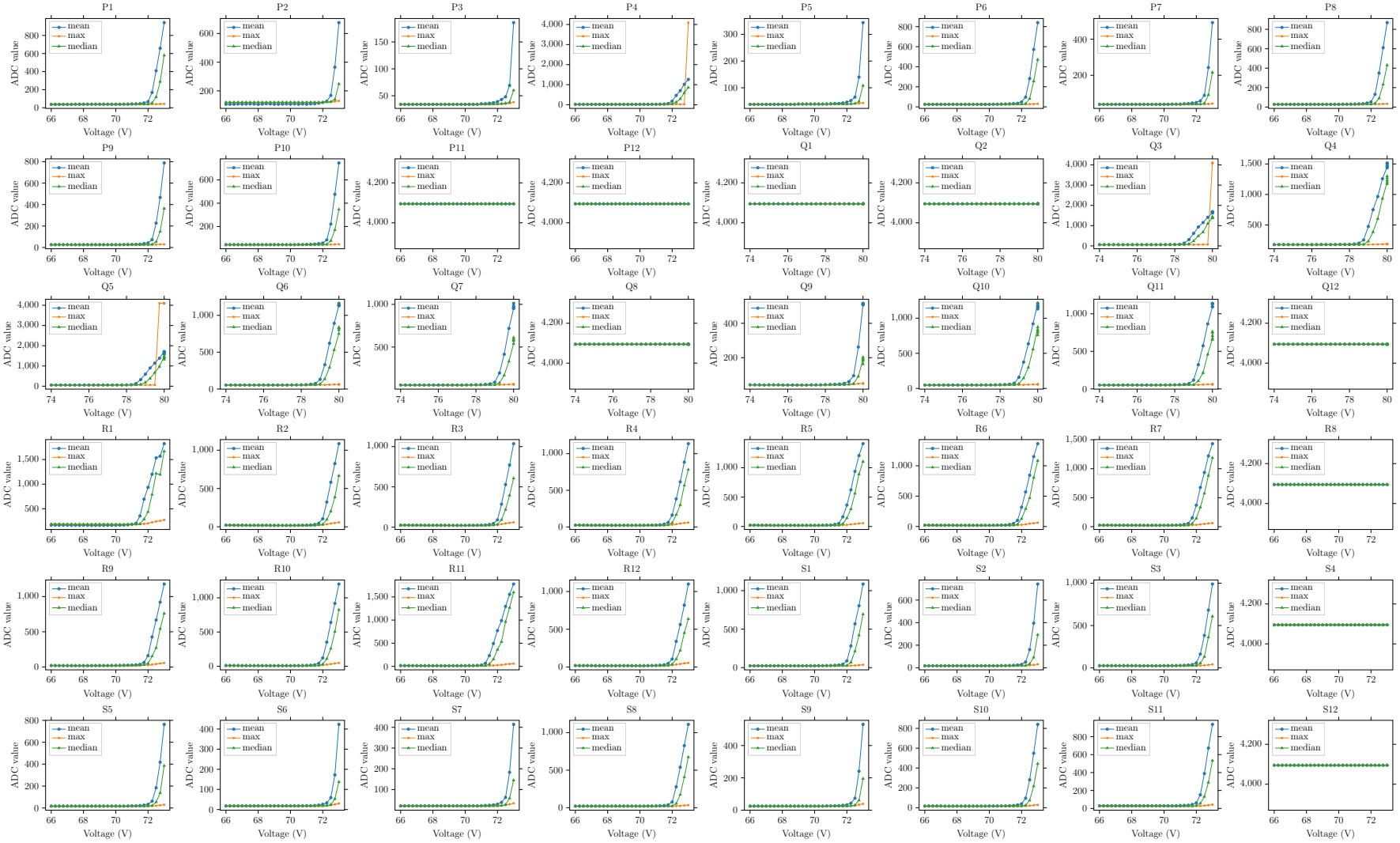

A.6 Single calibration data